Journal of Energy Chemistry 27 (2018) 1151–1169

Contents lists available at ScienceDirect

Journal of Energy Chemistry

journal homepage: www.elsevier.com/locate/jechem

http://www.journals.elsevier.com/journal-of-energy-chemistry/

Optical simulation of external quantum efficiency spectra of $CuIn_{1-x}Ga_xSe_2$ solar cells from spectroscopic ellipsometry inputs

Abdel-Rahman A. Ibdah[a], Prakash Koirala[a,*], Puruswottam Aryal[a], Puja Pradhan[a], Michael J. Heben[a], Nikolas J. Podraza[a], Sylvain Marsillac[b], Robert W. Collins[a]

[a] Department of Physics & Astronomy and Center for Photovoltaics Innovation & Commercialization, University of Toledo, Toledo 43606, Ohio, USA
[b] Virginia Institute of Photovoltaics, Old Dominion University, Norfolk 23529, Virginia, USA

ARTICLE INFO

Article history:
Received 25 August 2017
Revised 23 October 2017
Accepted 24 October 2017
Available online 1 November 2017

Keywords:
Solar cells
Thin-film
Ellipsometry
Spectroscopic
$CuIn_{1-x}Ga_xSe_2$ (CIGS)
Optical properties
Quantum efficiency
External
Simulation
Solar-cell

ABSTRACT

Applications of in-situ and ex-situ spectroscopic ellipsometry (SE) are presented for the development of parametric expressions that define the real and imaginary parts (ε_1, ε_2) of the complex dielectric function spectra of thin film solar cell components. These spectra can then be utilized to analyze the structure of complete thin film solar cells. Optical and structural/compositional models of complete solar cells developed through least squares regression analysis of the SE data acquired for the complete cells enable simulations of external quantum efficiency (EQE) without the need for variable parameters. Such simulations can be compared directly with EQE measurements. From these comparisons, it becomes possible to understand in detail the origins of optical and electronic gains and losses in thin film photovoltaics (PV) technologies and, as a result, the underlying performance limitations. In fact, optical losses that occur when above-bandgap photons are not absorbed in the active layers can be distinguished from electronic losses when electron-hole pairs generated in the active layers are not collected. This overall methodology has been applied to copper indium-gallium diselenide ($CuIn_{1-x}Ga_xSe_2$; CIGS) solar cells, a key commercialized thin film PV technology. CIGS solar cells with both standard thickness (>2 μm) and thin (<1 μm) absorber layers are studied by applying SE to obtain inputs for EQE simulations and enabling comparisons of simulated and measured EQE spectra. SE data analysis is challenging for CIGS material components and solar cells because of the need to develop an appropriate (ε_1, ε_2) database for the CIGS alloys and to extract absorber layer Ga profiles for accurate structural/compositional models. For cells with standard thickness absorbers, excellent agreement is found between the simulated and measured EQE, the latter under the assumption of 100% collection from the active layers, which include the CIGS bulk and CIGS/CdS heterojunction interface layers. For cells with thin absorbers, however, an observed difference between the simulated and measured EQE can be attributed to losses via carrier recombination within a ~0.15 μm thickness of CIGS adjacent to the Mo back contact. By introducing a carrier collection probability profile into the simulation, much closer agreement is obtained between the simulated and measured EQE. In addition to the single spot capability demonstrated in this study, ex-situ SE can be applied as well to generate high resolution maps of thin film multilayer structure, component layer properties and their profiles, as well as short-circuit current density predictions. Such mapping is possible due to the high measurement speed of <1 s per (ψ, Δ) spectra achievable by the multichannel ellipsometer.

1. Introduction

Spectroscopic ellipsometry (SE) is an optical analysis technique with broad applications in the study of thin films [1,2]. SE is based on the measurement of the polarization change that occurs upon oblique specular reflection of a polarized light beam from the interface(s) and surface of a substrate/thin-film structure. Thus, the technique has been utilized extensively in multilayer thin film photovoltaics (PV) technology for determination of the component layer thicknesses and optical properties of layers in devices [3]. In fact, the physical structure of the thin film PV device and the complex dielectric function spectra $\varepsilon(E)$ of the device materials, including semiconductors, transparent conducting oxides (TCOs), and metals, control the spectroscopic optical behavior of the device, e.g., the overall reflectance and transmittance spectra as well as the component layer absorbance spectra [4,5]. For all types of ma-

* Corresponding author.
E-mail addresses: prakash.koirala@rockets.utoledo.edu, prakash.koirala@utoledo.edu (P. Koirala).

https://doi.org/10.1016/j.jechem.2017.10.029
2095-4956/Published by Elsevier B.V. and Science Press on behalf of Science Press and Dalian Institute of Chemical Physics, Chinese Academy of Sciences.

terials, the spectra in $\varepsilon(E)$ with real and imaginary parts $\{\varepsilon_1(E), \varepsilon_2(E)\}$, respectively, can be understood in terms of one or more bound electron oscillators; for TCOs and metals one or more free charge carrier contributions are also added [2,6]. When applied in conjunction with least squares regression analysis methods, SE is a powerful tool, in principle, for extracting the photon energy independent parameters that characterize the PV device structure, including the layer thicknesses, as well as the bound and free carrier parameters that define the (ε_1, ε_2) spectra of the component materials [7]. In practice, however, least squares regression analysis of complicated multilayered PV stacks can present a considerable challenge if one seeks information simultaneously on both layer thicknesses and material optical characteristics. Considerable effort has focused on overcoming such a challenge in SE data analysis through independent determination of device-relevant (ε_1, ε_2) spectra given as parametric expressions.

SE is a valuable tool in PV research and development because it is non-invasive and contactless, and can be used for thin film analysis in various modes, including ex-situ off-line and on-line analysis, as well as in-situ and real time analysis. SE can be performed either from the film side in the conventional substrate configuration used for solar cells or from the glass side in the superstrate configuration [3,8–10]. It is also possible to perform both film-side and glass-side SE measurements, for example, when opaque back contacts do not cover the entire area of the device structure [10]. In this report, which presents SE analysis results for $CuIn_{1-x}Ga_xSe_2$ (CIGS) thin film solar cells in the substrate configuration, only a conventional film-side measurement is possible, however, due to the lack of transmittance through the opaque Mo back contacts that cover the soda lime glass substrate [3,11]. The goal of SE analysis in PV technology is to determine the component layer thicknesses, including those of interface and surface roughness layers, as well as the (ε_1, ε_2) spectra of the component materials of the solar cell [3]. Once this fundamental structural and optical information is determined by SE, device performance information can be predicted that describes the operational characteristics of the solar cell. First, one can predict the maximum external quantum efficiency (EQE) that is possible for the given solar cell stack specifications, i.e., its layer thicknesses, and the (ε_1, ε_2) spectra of the component layers. This prediction is based on the identification of the active component layers and often on the assumption of specular reflection and transmission conditions at interfaces, as described in previous ex-situ SE studies [12,13]. The SE methodology for solar cell characterization and the EQE predictions can also be expanded to include light scattering at rough interfaces and surfaces if desired [14–16]. By simulating the EQE for variations from the deduced structure or in the optical properties, one can identify approaches for improving the short-circuit current density (J_{SC}) in a solar cell expeditiously, thus avoiding trial-and-error approaches. Second, from the fundamental structural and optical information, the spectra in the reflectance from the solar illumination side can be predicted [10–13]. This prediction is helpful, for example, for determination of the benefits of anti-reflection coatings (ARCs), as well as for optimization of the anti-reflection coating stack design [11,17].

The EQE simulations described here, based on the SE analysis of standard high-performance CIGS solar cells, apply the assumption that all carriers photo-generated within the active layers of the cell are collected without recombination losses. Any differences between the simulated EQE obtained using input parameters from SE analysis and the experimental EQE from the measurement of a completed solar cell can provide information on possible breakdowns of the assumptions applied in the simulations, as has been described in studies of different thin film PV technologies [10,18–20]. Specifically, lower measured EQE values compared with the simulation can be attributed to losses due to recombination of carriers generated by photons absorbed within the active layers. Higher measured EQE values can be attributed to gains by light scattering and breakdown in the assumption used here of specularly reflecting and transmitting interfaces. Light scattering is generated by roughness with structural scales on the order of the probing light wavelength, whereas roughness with scales much less than the wavelength can be treated within a specular analysis as a layer with (ε_1, ε_2) spectra determined by an effective medium of underlying and overlying materials [1–3,7]. The spectral dependences of the CIGS solar cell losses and gains provide insights into these processes [20–22]. Here, SE analysis results of CIGS solar cells without and with ARCs as well as with different CIGS absorber layer thicknesses are described. EQE simulations based on these results are presented and compared to measurements for insights into cell optimization and carrier collection.

As a first step in performing the EQE simulations of this study, the parametric versions of the (ε_1, ε_2) spectra of the CIGS solar cell components are obtained [11]. The components studied here include the sputtered Mo, ZnO, and ZnO:Al back and top contact layers, the thermally evaporated CIGS layers having different Ga contents, the chemical bath deposited CdS, and electron beam evaporated ARC components. SE measurements of these components were performed in idealized sample structures that provide the (ε_1, ε_2) spectra and give insights into the oscillator models required to describe these spectra over the operational range of the solar cell with a minimum number of variable parameters [3,6]. For critical thin film material components, these SE measurements were performed in-situ and in real time to obtain more accurate information on the sample structure, which in turn enables more accurate room temperature (ε_1, ε_2) spectra after cooling the sample (when depositions occur at elevated temperatures). In addition, these in-situ measurements avoid oxidation of the surfaces which, if unrecognized, can lead to distortions of the (ε_1, ε_2) spectra. Using this complex dielectric function database, complete solar cells are measured by ex-situ SE and analyzed by least squares regression to extract thicknesses and key properties of the materials such as absorber Ga content that are included as photon energy independent variables in the analysis [3,20,22]. The SE analyses enable EQE simulations based on the assumptions described in the previous paragraph, and the simulations and measurements are compared in detail. Such comparisons reveal excellent agreement for standard high efficiency devices and enable optimization of single and multilayer ARCs [11,17]. The comparisons also provide insights into the challenges of thinning the CIGS layer motivated by the prospects of higher deposition throughput and reduced materials cost.

2. Experimental

The CIGS absorber layer in the substrate configuration serves as the foundation of one of the thin film PV technologies that has been successfully commercialized. Laboratory scale record cell efficiencies for this technology currently exceed 22% [23]. The CIGS solar cells of the study presented here apply the absorber layer deposition approach that yields the highest laboratory efficiency, namely three-stage co-evaporation of Cu, In, Ga, and Se [24]. In this study, intended 2.2 μm standard thickness and 0.5 μm reduced thickness CIGS absorber layers were deposited on molybdenum (Mo) coated soda lime glass (SLG). A thin CdS window layer deposited on top of the CIGS forms the heterojunction. The complete device structure includes the following component layers (with deduced effective thicknesses defined as the film volume/area) deposited on SLG: two-step dc-sputtered Mo back contact (~0.8–1.0 μm), CIGS absorber layer (~2.2 μm or 0.5 μm), chemical-bath-deposited (CBD) CdS (~50–100 nm), rf-sputtered transparent conducting oxide bilayer of ZnO/ZnO:Al (~50–100 nm/0.2–0.3 μm),

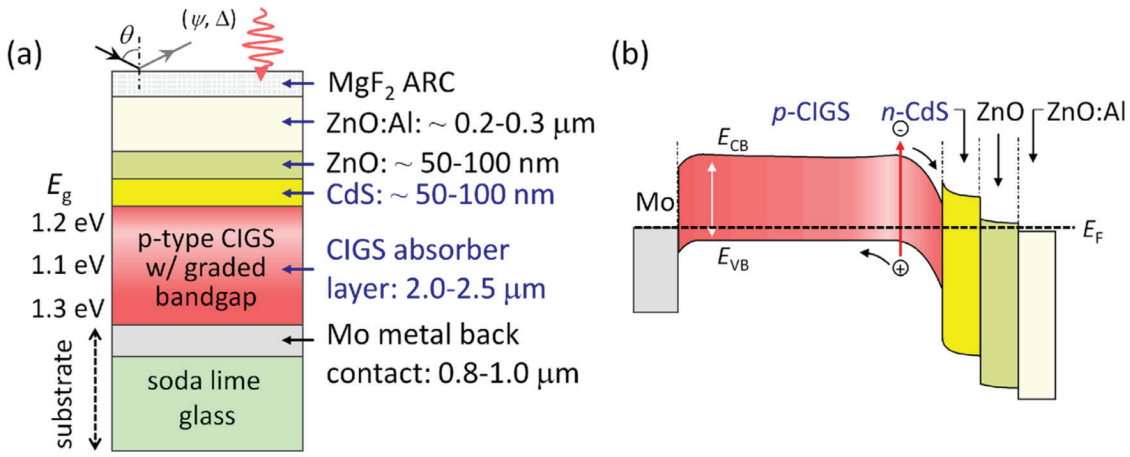

Fig. 1. (a) Schematic of the standard CIGS solar cell whose components and performance are characterized in this study of external quantum efficiency (EQE) spectra. The substrate is soda lime glass coated with a Mo back contact layer, the junction is CIGS/CdS, the top transparent conducting contact is a ZnO/ZnO:Al bilayer, and when applied, the anti-reflection coating (ARC) is MgF_2; (b) Schematic band diagram for the solar cell of (a) under open circuit conditions.

and electron beam evaporated Ni/Al/Ni grids. The total cell area was 0.5 cm^2, as defined by mechanical scribing [11]. An ARC consisting of a single layer of MgF_2 was then optimized through optical modeling and deposited in an electron beam evaporation system. The resulting multilayer structure schematic is shown in Fig. 1(a). Fig. 1(b) depicts a schematic band diagram of the solar cell at open circuit.

Starting from the SLG/Mo back contact structure, the interfaces and surface of the CIGS solar cell are quite rough, resulting in a complicated multilayer structural model for optical analysis [11,20–22,25]. Thus, the solar cell structure introduces considerable uncertainties if used for the determination of the (ε_1, ε_2) spectra for database applications. As a result, it is advantageous to generate and measure sample structures that are closer to ideal, by depositing individual CIGS solar cell component materials on smooth substrates that avoid interface roughness and in thinner layers that minimize the development of surface roughness. Real time, in-situ, and ex-situ SE methods are used for the determination of (ε_1, ε_2) spectra for these sample structures. Possible substrate and thickness dependences must be considered, however, when smooth substrates and thin layers are used for the database. Such dependences may lead to (ε_1, ε_2) spectra of the database that are not relevant for SE analysis of the multilayer devices. This suggests the importance of measuring the effects of substrate and thickness on (ε_1, ε_2) spectra in structures that are closer to ideal than the device itself. The ultimate goal is to develop and apply a physics-based analytical form for the (ε_1, ε_2) spectra that can account for variations due to the substrate and thickness. For example, one can use critical point energies that vary due to stress or broadening parameters that vary due to grain size effects, in addition to an effective medium theory to account for voids or density deficits [26,27]. Thus, setting up an accurate and relevant complex dielectric function database for devices can entail considerable background work. Confidence in the relevance and validity of the database can be obtained through studies that apply SE-deduced optical models to analyze complete solar cell structures and predict solar cell performance [19–22].

For the solar cells of this study, the first thin film component material to be deposited is Mo which is dc magnetron sputtered as a bilayer onto SLG held at a nominal substrate temperature of 250 °C [28,29]. The target-to-substrate distance of the sputtering system is 20 cm. Prior to bilayer deposition, a base pressure lower than 10^{-7} Torr is obtained and pre-sputtering is performed for 2 min. For both Mo layers of the process, a dc sputtering power of 150 W is applied to a pure Mo target 3 inches in diameter. A relatively thin Mo layer (~0.1 μm) is deposited as the first layer using an Ar pressure of ~15 mTorr and an Ar flow of ~140 sccm. A thicker second layer (~0.8 μm) is deposited next using a lower Ar pressure of 4 mTorr and Ar flow of 30 sccm. For this thicker layer, the deposition pressure was optimized for low Mo resistivity and adequate Na diffusion from the glass through the Mo layer into the overlying CIGS. For both Mo layers of the structure, the thicknesses are sufficiently large to ensure optical opacity over the photon energy range of the SE and EQE measurements. For the Mo thin film optical study, however, single layer depositions were performed on 22–23 nm thick thermal oxide coated crystalline silicon (c-Si) wafers due to their flatter surfaces. It is expected that the Mo films grow similarly on the underlying pure thermal SiO_2 and the SLG. The process variable in this optical property study was the nominal substrate temperature which ranged from room temperature to 385 °C, and enabled identification of 200 °C–250 °C as the optimum for solar cells. All other deposition parameters in this study were the same as those of the second component of the Mo bilayer used in the solar cell. Mo thin films with a reduced thickness range of 0.43–0.50 μm were used for the optical measurements since the (ε_1, ε_2) spectra were found to be essentially independent of thickness beyond ~0.5 μm. Based on this discussion, the (ε_1, ε_2) spectra for the 250 °C Mo deposition deduced from in-situ SE measurements at room temperature resulting from the optical property study are believed to be characteristic of the top most region of the Mo back contact used in the CIGS solar cells. Thus, these (ε_1, ε_2) spectra are applied in SE analysis of the complete solar cells.

Deposition of the CIGS, which is the second thin film material of the solar cell, is initiated with the first stage of the three-stage process. This first stage is performed on the Mo bilayer coated SLG substrate at a temperature of 400 °C and involves co-evaporation of In, Ga, and Se at rates of 0.20 nm/s, 0.06 nm/s, and 2.0 nm/s, respectively [11,30]. Once the desired $(In_{1-x}Ga_x)_2Se_3$ film thickness is reached, which is ~70% of the total desired CIGS effective thickness, the first stage is terminated by reducing the source temperatures for In and Ga to stop co-evaporation. The substrate temperature is then increased to 570 °C over a time of 20 min to initiate the second stage. At this point, the source temperature of Cu is set to obtain an evaporation rate of 0.17 nm/s, while maintaining continuous co-evaporation of Se. As determined by the detection of the Cu-poor to Cu-rich transition, defining the second stage end-point for CIGS, Cu evaporation is terminated. In order to obtain a final Cu-poor CIGS layer in the third stage, In and Ga are again deposited using the first stage rates while maintaining con-

tinuous Se flux and 570 °C substrate temperature. At the endpoint of the third stage, as defined by the Cu-rich to Cu-poor transition, the In and Ga sources are cooled to terminate co-evaporation. During the three stages of CIGS deposition, the In, Ga, and Cu fluxes are controlled by electron impact emission spectroscopy calibrated by a quartz crystal monitor; the evaporation crucibles are heated thermally; and the substrate temperature is measured by a thermocouple attached to the back side of the sample. For the optical studies, CIGS films ~60 nm thick were deposited onto native oxide covered c-Si wafers by one stage co-evaporation using rates yielding alloy compositions of $x=[Ga]/\{[In]+[Ga]\}=0.00$, 0.12, 0.26, 0.30, 0.37, and 0.48 with $y=[Cu]/\{[In]+[Ga]\}=0.90\pm0.03$ [30,31]. These films were measured in-situ by SE after cooling to room temperature. Although one might expect that the resulting (ε_1, ε_2) spectra are subject to possible thickness and substrate dependences in this case, the present and previous studies [31] have suggested that the spectra obtained for the very thin films on smooth Si wafer substrates are also relevant and applicable for much thicker CIGS films (up to 2.2 μm) on Mo coated SLG substrates.

The purpose of the third material component of the solar cell stack, *n*-type CdS, is to form a *p*-*n* junction with the underlying *p*-type CIGS. In the fabrication of CIGS solar cells, this layer was deposited by chemical bath deposition (CBD) to a thickness of ~50–100 nm on top of the CIGS layer [11,30]. The CBD process involves first rinsing the SLG/Mo/CIGS structures with deionized water and drying with nitrogen, and then immersing the structures for 10 min with a temperature ramp from 40 °C to 65 °C in an optimized 500 mL solution containing 1 M ammonium hydroxide, 0.1 M cadmium acetate, and 0.0015 M thiourea. Thus, the Cd:S molar ratio for the solar cell depositions is $x=[Cd]/[S]=67$. In this solution, cadmium acetate acts as a source of Cd^{2+} ions, thiourea acts as a source of S^{2-}, and ammonium hydroxide acts as a catalyst. The CdS layer thickness required for a CIGS solar cell is related to the surface roughness of the CIGS absorber. A thicker CdS layer is needed to completely cover a larger CIGS roughness layer and avoid cell shunting. For optical measurements, CdS thin films were deposited onto native oxide covered Si wafers by CBD for 18 min, yielding films with effective thicknesses ranging from 30 to 95 nm. The bath compositions explored in the optical study were as follows: ammonium hydroxide at 1.5 M, thiourea at 0.0075 M, and cadmium acetate at the five different values of 0.0015 M, 0.0030 M, 0.0045 M, 0.0060 M, and 0.0075 M, yielding $x=0.2$, 0.4, 0.6, 0.8, and 1.0, respectively. A consistent variation in the (ε_1, ε_2) spectra as measured by ex-situ SE is observed over this range, as will be described in the next section.

The ZnO and ZnO:Al films are the fourth and fifth material components of the CIGS solar cell structure studied here and are deposited on the SLG/Mo/CIGS/CdS structures at room temperature in a radio-frequency (rf) magnetron sputtering system of design similar to that used for Mo [11]. These films are deposited from 3 inch diameter ZnO and ZnO/Al_2O_3 (98/2 wt%) ceramic targets, respectively. Prior to each film deposition, the targets are pre-sputtered for 10 min. The ZnO depositions were performed using an Ar gas pressure of 4 mTorr and flow of 30 sccm, a rf sputtering power of 80 W, and a sputtering time of 60 min. The ZnO:Al depositions were performed using an Ar gas pressure of 2 mTorr and flow of 14 sccm, a rf sputtering power of 150 W, and a sputtering time of 90 min. For the optical studies, the films were deposited onto thermal oxide covered c-Si wafers of pre-determined oxide layer thicknesses of ~27 nm and measured by ex-situ SE. Various substrate temperatures of 20 °C, 50 °C, 100 °C, and 150 °C (nominal values) were used to explore the effects on the (ε_1, ε_2) spectra of the ZnO and ZnO:Al films. For both the Mo and ZnO/ZnO:Al deposition systems, substrate temperature was calibrated in separate studies using a native oxide covered Si wafer, based on the photon energy

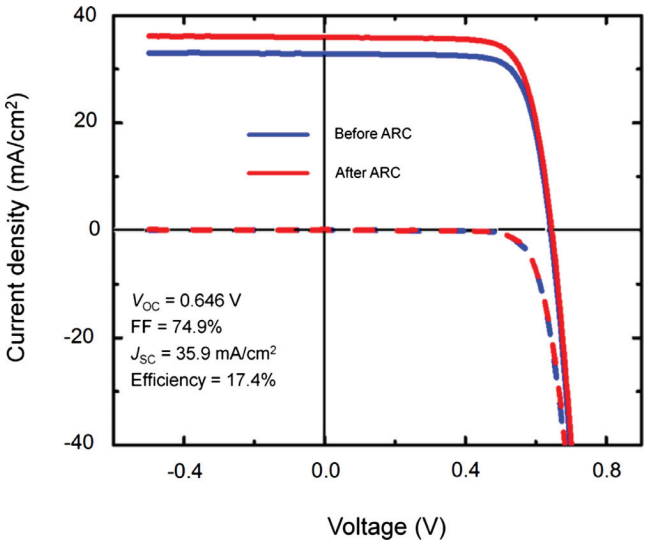

Fig. 2. (Current density)-voltage curves under AM 1.5 illumination (solid lines) and in the dark (broken lines) for a CIGS solar cell having the structure shown in Fig. 1 and incorporating a CIGS absorber with a standard thickness of 2.2 μm. Results are shown before and after deposition of an MgF_2 ARC.

locations of the Si E_1 and E_2 critical points [29]. The equation relating the calibrated temperature T_c and the nominal temperature T_n is $T_c = 20\ °C + 0.787(T_n - 20\ °C) + (3.048\times10^{-4}\ /°C)\ (T_n - 20\ °C)^2$. Thus, the difference $\Delta T = T_n - T_c$ increases monotonically from 0 °C to 36 °C over the range from $T_n = 20$ °C to 385 °C.

For the solar cells, optimized MgF_2 ARCs were applied to the completed SLG/Mo/CIGS/ CdS/ZnO/ZnO:Al structures by electron-beam evaporation [11]. For optical measurements, thin films of MgF_2, HfO_2, ZrO_2, TiO_2, and SiO_2, serving as possible components of multilayer ARCs, were deposited to effective thicknesses within the range of 33–198 nm using the same electron-beam evaporation system. For all films prepared in this system, a base pressure of less than 10^{-6} Torr was obtained prior to the depositions. No oxygen gas was added during the oxide depositions. Al_2O_3 was deposited in an atomic layer deposition system to an effective thickness of 55 nm. Substrates of c-Si with pre-determined oxide layer thicknesses of ~27 nm were used for all ARC depositions for the optical measurements.

The SE-EQE study presented in Section 3 includes results for CIGS solar cells with both standard and thin absorber layers before and after ARC deposition [11]. The performance characteristics are shown in Fig. 2 for the best CIGS solar cell fabricated in this study having the standard absorber layer thickness of 2.2 μm. The light and dark (current density)-voltage (*J*-*V*) curves of the solar cell shown in Fig. 2 correspond to results obtained before and after the deposition of the ARC. Upon application of the ARC, the solar cell efficiency is observed to increase from $\eta = 16.4\%$ to 17.4%. Optical studies of CIGS cells with standard absorber layer thicknesses and a cell with a reduced absorber thickness of ~0.5 μm have been performed and the results are presented in this study as well. For the cell with the thin absorber, addition of the ARC led to an increase in efficiency from 9.9% to 10.5%. The motivation for developing CIGS solar cells with thin absorber layers is to reduce materials costs and increase throughput in module manufacturing. The complete solar cells were investigated using ex-situ SE, which was performed from the film side. For optical measurements of the completed solar cells without and with ARCs, the ellipsometry angles (ψ, Δ) were obtained versus photon energy over the range from 0.9 to 4.0 eV at an angle of incidence of 70° (V-VASE, J. A. Woollam Co.). An ultimate goal of this study with respect to thin film metrology is to develop structural/optical models and analysis

methods that can be used in on-line and module mapping applications.

3. Results and discussion

3.1. Complex dielectric functions of materials

A common description of the frequency (ω) dependent linear response of a material to an electromagnetic wave having a time dependence $\exp(i\omega t)$ is the complex index of refraction $N(E)=n(E)-ik(E)$, where $E=\hbar\omega$ is the photon energy [1,2]. A second approach is through the complex dielectric function $\varepsilon(E)=\varepsilon_1(E)-i\varepsilon_2(E)$. The relationship between the two descriptions is $N(E)=[\varepsilon(E)]^{1/2}$ so that:

$$\varepsilon_1 - i\varepsilon_2 = (n-ik)^2 \tag{1}$$

Expanding N^2 and equating the real and imaginary parts on both sides of the equation, give:

$$\varepsilon_1 = n^2 - k^2; \quad \varepsilon_2 = 2nk \tag{2}$$

Inverting these equations yields:

$$n = \{1/2[|\varepsilon| + \varepsilon_1]\}^{1/2}; \quad k = \{1/2[|\varepsilon| - \varepsilon_1]\}^{1/2}; \quad |\varepsilon| = (\varepsilon_1^2 + \varepsilon_2^2)^{1/2} \tag{3}$$

Various parametric forms for the photon energy dependence of ε have been developed for different materials with one motivation being least squares regression analysis of SE data. These forms are based on physical principles that describe the interaction of the electromagnetic wave with the electrons in the energy states of the material [6]. The simplest form is based on the treatment of an electron in the solid as a damped harmonic oscillator driven by the optical electric field. For electrons that are bound in filled valence band states with their transition energies occurring within the photon energy range of measurement, the damped, driven harmonic oscillator description yields a Lorentz oscillator term in the expression for $\varepsilon(E)$. In contrast, if the transitions occur well outside the spectral range of measurement so that absorption in negligible, then a Sellmeier term in the expression for $\varepsilon_1(E)$ can be used, without an $\varepsilon_2(E)$ contribution. For electrons that are free in partially-filled conduction band states, a Drude term in the expression for $\varepsilon(E)$ can be used.

Considering a single material that combines all types of transitions, then the real and imaginary parts of the complex dielectric function can be expressed as [6]:

$$\varepsilon_1(E) = \varepsilon_{1o} + \sum_{n=1}^{N_D} \mathrm{Re}\{\varepsilon_{D,n}(E)\} + \sum_{n=1}^{N_S} A_{S,n}{}^2 (E_{S,n}{}^2 - E^2)^{-1} + \sum_{n=1}^{N_{TL}} \mathrm{Re}\{\varepsilon_{TL,n}(E)\} + \sum_{n=0}^{N_{CP}-1} \mathrm{Re}\{\varepsilon_{CP,n}(E)\} \tag{4}$$

$$\varepsilon_2(E) = \sum_{n=1}^{N_D} \mathrm{Im}\{\varepsilon_{D,n}(E)\} + \begin{cases} \varepsilon_{2,B}(E_t)\exp[(E-E_t)/E_u] & E < E_t \quad (5) \\ \sum_{n=1}^{N_{TL}} \mathrm{Im}\{\varepsilon_{TL,n}(E)\} + \sum_{n=0}^{N_{CP}-1} \mathrm{Im}\{\varepsilon_{CP,n}(E)\} & E \geq E_t \quad (6) \end{cases}$$

In Eq. (4), ε_{1o} represents a constant (i.e., non-dispersive) contribution to the real part of $\varepsilon(E)$. In addition $\varepsilon_{D,n}(E)$, with real (Re) and imaginary (Im) parts in Eq. (4) and Eqs. (5)–(6), respectively, represents the nth Drude expression in the sum according to [6]:

$$\varepsilon_{D,n}(E) = -\frac{A_{D,n}{}^2}{E^2 + i\Gamma_{D,n}E} \tag{7}$$

whereby $\varepsilon(E)$ incorporates a sum of N_D such expressions, one for each distinct collection of free carriers, which may include electrons and/or holes. Here, $A_{D,n}$ and $\Gamma_{D,n}$ are Drude amplitude and broadening parameters in the nth expression, respectively. In an alternative expression for the Drude term, $A_{D,n}$ and $\Gamma_{D,n}$ are replaced by the resistivity ρ_n and mean free time τ_n, leading to the form:

$$\varepsilon_{D,n}(E) = -\frac{\hbar^2}{\varepsilon_0 \rho_n (\tau_n E^2 + i\hbar E)} \tag{8}$$

where ε_0 is the permittivity of free space and $\hbar = h/2\pi$ with h as Planck's constant. The third term of $\varepsilon_1(E)$ in Eq. (4) represents a sum of N_S Sellmeier expressions whose amplitudes are defined by $A_{S,n}$ and whose resonance energies $E_{S,n}$ must be located either below or above the photon energy range of $\varepsilon(E)$ to avoid singularities.

The fourth term in Eq. (4) describes a sum of a more general form of the Lorentz oscillator which has a low energy cut-off in $\varepsilon_2(E)$ at a bandgap E_G, which is the Tauc gap. Such a Tauc-Lorentz oscillator is most easily described through the imaginary part of $\{\varepsilon_{TL,n}(E)\}$ as in Eq. (6), given by [6]:

$$\mathrm{Im}\{\varepsilon_{TL,n}(E)\} = \left(\frac{E-E_G}{E}\right)^2 \left(\frac{A_{TL,n}E_{TL,n}\Gamma_{TL,n}E}{(E_{TL,n}{}^2 - E^2)^2 + \Gamma_{TL,n}{}^2 E^2}\right)\Theta(E-E_G) \tag{9}$$

with $\Theta(E-E_G)$ as a unit step function with a value of zero for $E \leq E_G$ and unity for $E > E_G$. In Eq. (9), $A_{TL,n}$, $E_{TL,n}$, and $\Gamma_{TL,n}$ are the amplitude, resonance energy, and broadening parameter for the Tauc-Lorentz oscillator. By setting $E_G = 0$, one can return to the simple form of the Lorentz oscillator whose imaginary part is the second term in brackets on the right side of Eq. (9). In Eq. (4), $\mathrm{Re}\{\varepsilon_{TL,n}(E)\}$ is determined by a Kramers-Kronig integral of Eq. (9). Although a single Tauc-Lorentz oscillator is typically used for amorphous semiconductors, one or more such oscillators, as indicated by the sum in Eqs. (4)–(6), can be used to describe the broad background absorption between the critical points of nano, poly, or single-crystalline solids.

Finally, the fifth term in Eq. (4) describes a sum of N_{CP} oscillators describing the critical points (CPs) in crystalline materials with a complex dielectric function expression for a single CP given by [6]:

$$\varepsilon_{CP,n}(E) = \frac{A_{CP,n}(\Gamma_{CP,n}/2)_n^{\mu}\exp(i\phi_n)}{[E_{CP,n} - E + i(\Gamma_{CP,n}/2)]_n^{\mu}} \tag{10}$$

where $A_{CP,n}$, $E_{CP,n}$, $\Gamma_{CP,n}$, ϕ_n, and μ_n are the amplitude, resonance energy, broadening parameter, phase, and exponent of the CP oscillator. The sum in Eqs. (4)–(6) ranges from zero to $N_{CP}-1$ in recognition of the fact that the lowest energy CP of a semiconductor, which is the fundamental bandgap, is assigned the subscript '0' by convention.

The two expressions for $\varepsilon_2(E)$, Eqs. (5) and (6), separate the exponential Urbach tail behavior below E_t from the bandgap absorption onset above E_t. Urbach behavior is observed below the lowest energy CP transitions with a resonance energy $E_{CP,0} = E_t$ based on the assumption $E_{CP,0} \leq E_G$. If instead the lowest energy transitions are associated with a Tauc-Lorentz oscillator, then the separation energy E_t is set to a value slightly above E_G to enable continuity of $\varepsilon_2(E)$. In Eq. (5), E_u describes the Urbach tail slope and $\varepsilon_{2,B}(E_t)$ is the combined CP and Tauc-Lorentz bound electron contribution to ε_2 at E_t that ensures continuity between the two segments of $\varepsilon_2(E)$. It should be noted that the contribution of the Urbach absorption to $\varepsilon_1(E)$ is neglected in Eq. (4). This is a reasonable approximation in crystalline materials; however, for amorphous materials with the gap energy E_G as defined by the Tauc-Lorentz oscillator expression, the $\varepsilon_1(E)$ contribution is

Table 1. Photon energy independent parameters that describe the dielectric function spectra (ε_1, ε_2) of the component layers of the CIGS solar cell over the photon energy range from 0.9 to 4.0 eV. Parameter definitions are given in Eqs. (2)–(10). The resulting (ε_1, ε_2) spectra are used in SE analysis of complete solar cells and EQE simulations.

Parameter	Mo	CIGS ($x=0.3$)	CdS	ZnO	ZnO:Al
ε_{1o}	4.594	0.586	1.000	1.000	2.093
ρ_1 (Ω cm)	1.012×10^{-5}	–	–	–	88.83×10^{-5}
τ_1 (*fs*)	12.35	–	–	–	5.088
ρ_2 (Ω cm)	37.40×10^{-5}	–	–	–	–
τ_2 (*fs*)	0.100	–	–	–	–
$A_{CP,0}$	13.28	1.277	5.036	2.414	3.093
$E_{CP,0}$ (eV)	1.594	1.194	2.381	3.323	3.705
$\Gamma_{CP,0}$ (eV)	1.050	0.077	0.265	0.237	0.301
ϕ_0 (degree)	−41.85	−33.04	−27.10	−25.04	−1.84
μ_0	1.000	0.302	0.167	0.538	0.307
$A_{CP,1}$	7.253	1.836	19.480	103.94	–
$E_{CP,1}$ (eV)	2.259	1.421	7.235	8.124	–
$\Gamma_{CP,1}$ (eV)	0.699	0.449	0.637	0.682	–
ϕ_1 (degree)	−54.54	3.410	62.55	121.84	–
μ_1	1.000	0.288	0.823	1.958	–
$A_{CP,2}$	14.79	3.484	–	–	–
$E_{CP,2}$ (eV)	4.245	2.939	–	–	–
$\Gamma_{CP,2}$ (eV)	1.392	0.615	–	–	–
ϕ_2 (degree)	28.86	−0.640	–	–	–
μ_2	1.000	0.869	–	–	–
$A_{CP,3}$	–	0.0938	–	–	–
$E_{CP,3}$ (eV)	–	3.755	–	–	–
$\Gamma_{CP,3}$ (eV)	–	0.516	–	–	–
ϕ_3 (degree)	–	159.21	–	–	–
μ_3	–	3.000	–	–	–
$A_{TL,1}$ (eV)	–	78.20	–	115.16	14.50
$E_{TL,1}$ (eV)	–	6.232	–	9.650	5.000
$\Gamma_{TL,1}$ (eV)	–	10.478	–	23.817	10.074
E_G (eV)	–	1.194	–	3.323	3.705
E_u (eV)	–	0.0582	–	–	–
$\varepsilon_2(E_t)$	–	0.334	–	–	–

stronger and the exponential integral form for this contribution has been provided elsewhere [6]. Considering CIGS with $x=0.30$ as an example, the Urbach tail contribution to $\varepsilon_1(E)$ is <0.1 as long as $|E-E_{CP,0}|>0.01$ eV. At the bandgap $E_{CP,0}$, the Kramers-Kronig integral involving the Urbach tail generates a divergence in $\varepsilon_1(E)$ due to the discontinuous derivative in $\varepsilon_2(E)$ at $E=E_{CP,0}$. As noted elsewhere, this divergence is of little consequence [6]; in the case of CIGS with $x=0.30$, the calculated ε_1 contribution increases to only ~0.4 for $|E-E_{CP,0}|\sim0.001$ eV.

Considering the crystallography of the solar cell component materials of Fig. 1, the crystal structure of CIGS is chalcopyrite, that of CdS and ZnO(:Al) is wurtzite, and that of MgF_2 is rutile. As a result, all four materials are uniaxially anisotropic in single crystal form, implying the existence of distinct ordinary and extraordinary complex dielectric functions for optical fields perpendicular and parallel to the unique *c*-axis of the crystal, respectively [32–35]. Because the anisotropy of the single crystal materials is relatively weak and because the materials exist as polycrystalline films in this study, the anisotropy is neglected in the SE materials and device analyses to be discussed and in the EQE simulations, as well. Although the angle of incidence is large in the SE measurements, refractions at the interfaces to the ambient for all but the ARC imply that the optical fields within the materials lie predominantly parallel to the film planes. Thus, any effects of anisotropy on the SE measurements are likely to be masked by a distribution of in-plane crystallite orientations which yield an isotropic average dielectric function. For the EQE measurements and simulations, a normal incidence configuration is used which is assumed to rely on this average dielectric function. For back contact Mo, the crystal structure is body-centered cubic and, thus, the polycrystalline Mo films are expected to be optically isotropic. Previous studies have detected in-plane optical anisotropy in thin film Mo at the SLG/Mo interface, attributed to angular variations in film microstructure [36]. Such effects, detected by rotating the sample, however, have not been observed at the near surfaces of the Mo films of the present study.

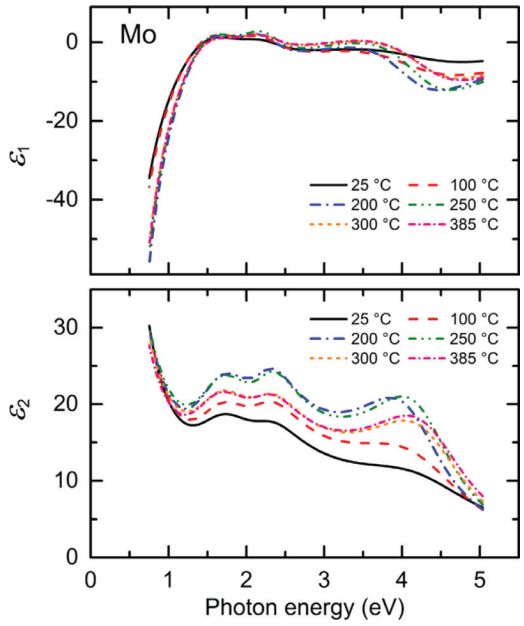

Fig. 3. Parametric expressions for the room temperature complex dielectric functions of magnetron sputtered Mo thin films deposited at nominal substrate temperatures of 25 °C, 100 °C, 200 °C, 250 °C, 300 °C, and 385 °C. These (ε_1, ε_2) spectra were deduced from in-situ SE data obtained on opaque films 0.43–0.50 μm thick. In the analysis, the SE data were corrected for surface roughness layers, each assumed to consist of a fixed 50–50 vol% Mo-void content. For parameterization, the (ε_1, ε_2) spectra were represented by a sum of two Drude components and three CP oscillators. The photon energy independent parameters that define the (ε_1, ε_2) spectra for the film deposited at 250 °C are given in Table 1.

Fig. 3 shows the best fit analytical forms of the complex dielectric functions of Mo thin films deposited at nominal values of the substrate temperature including 25 °C (room temperature), 100 °C,

Table 2. Critical point and Tauc-Lorentz oscillator parameters for CIGS alloys, as well as ε_{1o}, E_u, and $\varepsilon_2(E_t)$, described by second or third order polynomials in $\Delta x = x-0.30$, where x is the Ga composition. The values of fixed parameters are also provided. The expressions for the parameters are valid for $0 \le x < 0.5$ over the photon energy range of 0.9 eV $\le E \le$ 4.0 eV for ε_1 and $E_t < E \le 4$ eV for ε_2. Below E_t, ε_2 is given as an Urbach tail generated by E_u and $\varepsilon_2(E_t)$.

Oscillator, CIGS CP	Parameter	Expression in terms of x
CP,0 E_0(A,B)	$A_{CP,0}$	$-1.66(\Delta x)^2 - 0.860(\Delta x)+1.277$
	$E_{CP,0}$ (eV)	$-0.063(\Delta x)^2+0.547(\Delta x)+1.194$
	$\Gamma_{CP,0}$ (eV)	0.077
	ϕ_0 (degree)	$-5.411(\Delta x)^2 - 3.993(\Delta x) - 33.040$
	μ_0	0.302
CP,1 E_0(C)	$A_{CP,1}$	$-16.30(\Delta x)^3+7.320(\Delta x)^2+3.352(\Delta x)+1.836$
	$E_{CP,1}$ (eV)	$-0.388(\Delta x)^2+0.487(\Delta x)+1.421$
	$\Gamma_{CP,1}$ (eV)	0.449
	ϕ_1 (degree)	$-412.96(\Delta x)^2+78.14(\Delta x)+3.410$
	μ_1	0.288
CP,2 E_1(A)	$A_{CP,2}$	$-0.953(\Delta x)^2 - 4.256(\Delta x)+3.484$
	$E_{CP,2}$ (eV)	$-0.049(\Delta x)^2+0.138(\Delta x)+2.939$
	$\Gamma_{CP,2}$ (eV)	$-2.840(\Delta x)^2-0.264(\Delta x)+0.615$
	ϕ_2 (degree)	$85.44(\Delta x)^2 - 167.64(\Delta x)-0.640$
	μ_2	$-1.02(\Delta x)^2+1.148(\Delta x)+0.869$
CP,3 E_1(B)	$A_{CP,3}$	$0.239(\Delta x)^2-0.0656(\Delta x)+0.0938$
	$E_{CP,3}$ (eV)	$0.278(\Delta x)^2+0.427(\Delta x)+3.755$
	$\Gamma_{CP,3}$ (eV)	0.516
	ϕ_3 (degree)	159.21
	μ_3	3.000
Tauc-Lorentz	$A_{TL,1}$ (eV)	$137.3(\Delta x)^2+134.0(\Delta x)+78.2$
	$E_{TL,1}$ (eV)	6.232
	$\Gamma_{TL,1}$ (eV)	$-88.91(\Delta x)^3+2.344(\Delta x)^2+14.242(\Delta x)+10.478$
	E_G (eV)	$-0.063(\Delta x)^2+0.547(\Delta x)+1.194$
Constant ε_1 offset	ε_{1o}	$1.008(\Delta x)^2 - 3.308(\Delta x)+0.586$
Urbach tail	E_u (eV)	$0.499(\Delta x)^2+0.260(\Delta x)+0.0582$
	$\varepsilon_2(E_t)$	$0.886(\Delta x)^2+0.311(\Delta x)+0.334$

200 °C, 250 °C, 300 °C, and 385 °C and measured at room temperature [29]. In order to characterize the film structure and extract these (ε_1, ε_2) spectra, real time SE measurements were performed during film growth at an angle of incidence within the range of 69.89° to 69.92° with maximum observed confidence limits of ±0.05°. A rotating-compensator multichannel ellipsometer (M2000DI, J.A. Woollam Co.) with a potential photon energy range of 0.75 to 6.5 eV was used. Spectra in the ellipsometry angles (ψ, Δ) were collected with an acquisition time of 3 s. Real time SE data were collected throughout the growth of each Mo film and in-situ SE was performed for the final Mo film at room temperature. After the film reached opacity, a single-layer optical model was used to analyze the real time SE data and determine the evolution of the surface roughness layer thickness d_s on the film. The roughness layer was modeled as a 50/50 vol% mixture of (bulk Mo)/void with its dielectric function represented by applying the Bruggeman effective medium approximation. It is assumed that the roughness thickness deduced at the end of deposition does not change when the Mo film is cooled from the elevated deposition temperatures, and this enables extraction of the room temperature (ε_1, ε_2) spectra by numerical inversion.

These complex dielectric functions obtained by inversion are fit with a parametric model described by Eqs. (4)–(6) consisting of a constant real contribution ε_{1o}, two Drude terms, and three CP oscillators with resonance energies of 1.59, 2.26, and 4.25 eV for the sample deposited at 250 °C [29]. Because of the broad CP features, the exponents are set to unity, yielding characteristics of Lorentzian lineshapes. The parameters of this model are given by the first data column in Table 1. Two Drude terms may arise since Mo is a compensated metal with both electron and hole contributions to the dielectric response [37]. It is also possible that the broad Drude term with shorter τ also serves to simulate the broad background between the interband CPs. Because of the strong Drude terms, Eq. (5) describing the Urbach tail is not needed. The results in Fig. 3 suggest that the films deposited at 200 °C and 250 °C exhibit the strongest amplitude dielectric function as well as the sharpest CPs and sharpest drop in $\varepsilon_1(E)$ with decreasing photon energy in the near-infrared range. These effects

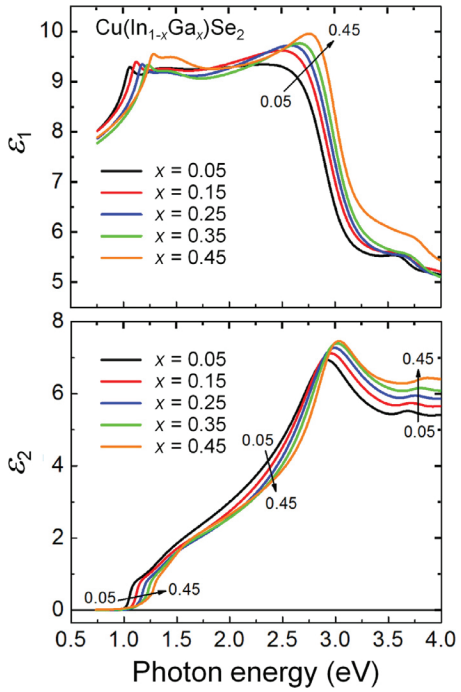

Fig. 4. Room temperature complex dielectric function spectra (ε_1, ε_2) plotted over the photon energy range from 0.75 to 4.00 eV for CIGS films with [Ga]/{[*In*]+[*Ga*]} atomic ratios x of 0.05, 0.15, 0.25, 0.35, and 0.45. These parametric results were developed based on best fits to (ε_1, ε_2) spectra obtained from in-situ SE data. From the fits, a parametric model was adopted including four critical point oscillators, a broad background Tauc-Lorentz oscillator, and an Urbach tail. The parameters of these (ε_1, ε_2) contributions are expressed as polynomial functions of $\Delta x = x - 0.30$ as presented in Table 2. The (ε_1, ε_2) parameters for $x = 0.30$ are provided as the second data column in Table 1.

are likely resulting from the highest density Mo film structure and the largest grain size, the latter generating the longest excited state lifetimes for the CPs as well as the lowest resistivity and longest mean free time for the Drude components.

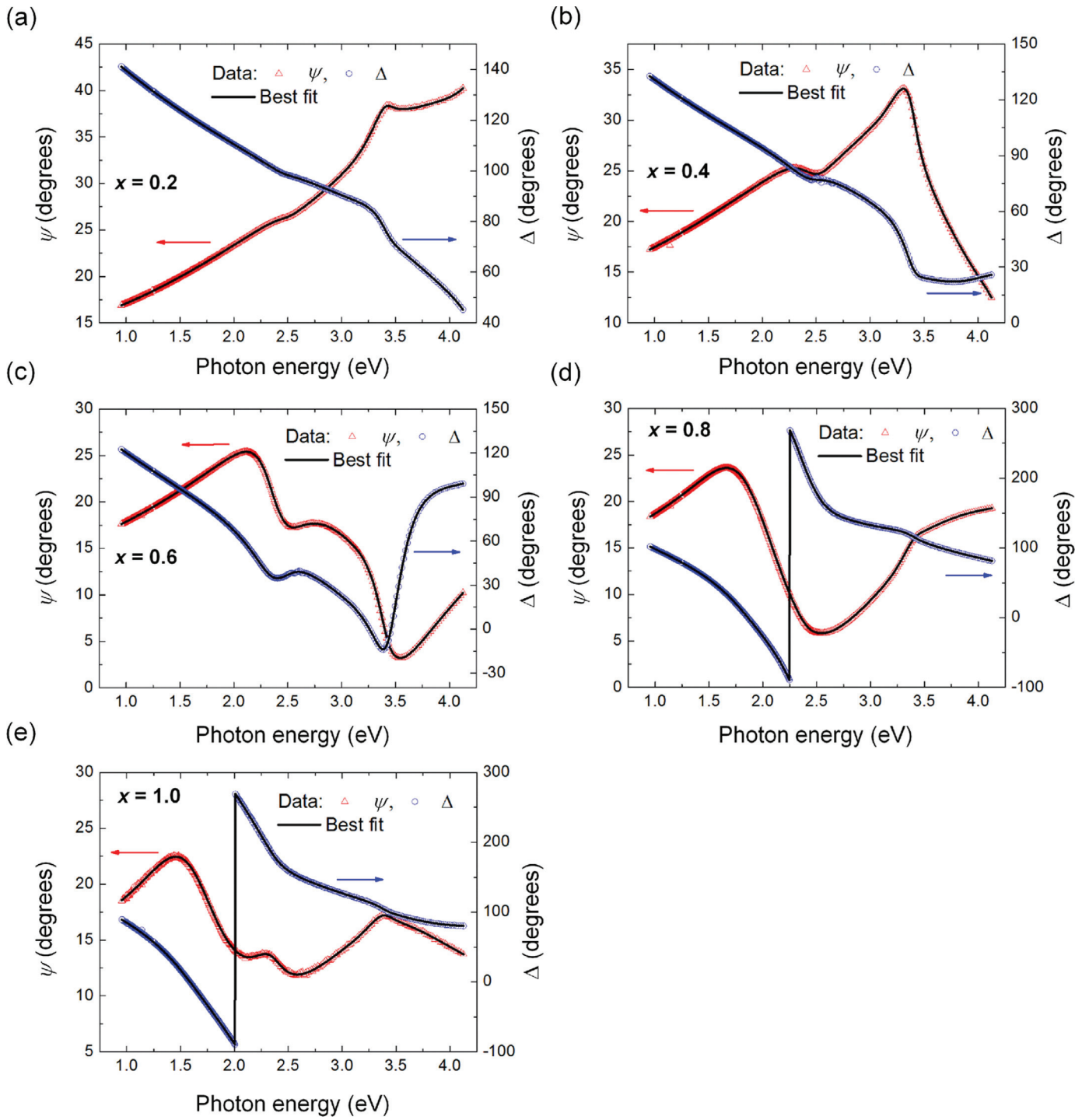

Fig. 5. Experimental ellipsometry angles (ψ, Δ) plotted as functions of photon energy along with the best fits (lines) for CdS films prepared by chemical bath deposition using different molar ratios of Cd to S precursors (x): (a) $x=0.2$, (b) $x=0.4$, (c) $x=0.6$, (d) $x=0.8$, (e) $x=1.0$. The SE data were collected ex-situ at room temperature at an angle of incidence of 65° immediately after removal from the bath and cooling from the bath temperature. Through additional analysis steps including inversion and constrained (ε_1, ε_2) fitting, parametric expressions for the complex dielectric functions are obtained as shown in Fig. 6.

Similar real time and in-situ SE approaches were applied to obtain inverted (ε_1, ε_2) spectra for CIGS films which in turn were fit in order to establish a parametric expression for the (ε_1, ε_2) spectra suitable for arbitrary Ga composition x. Thin films with different Ga contents $x=0.00$, 0.12, 0.26, 0.30, 0.37, and 0.48, for fixed $y=0.90\pm0.03$, were deposited onto native oxide covered c-Si wafers using a one stage co-evaporation process at a substrate temperature of 570 °C [11,30,31]. The deposition time was controlled to 50–60 s with a substrate shutter. In this time, the thickness of each deposited CIGS film was very thin, ~50–60 nm, in order to ensure a smooth film surface and to suppress possible effects of compositional non-uniformity versus depth into the film. Real time SE was performed during CIGS film growth with an acquisition time of 0.1 s. Analysis of the real time SE data provided the evolution of the film structure in terms of bulk and surface roughness layer thicknesses. Upon completing film fabrication and cooling the sample, in-situ SE was performed at room temperature for determination of the (ε_1, ε_2) spectra, using a 9.0 s acquisition

time for greater signal averaging. The composition identifying the sample was measured ex-situ using energy dispersive X-ray spectroscopy after removal of the sample from the deposition system.

The room temperature (ε_1, ε_2) spectra obtained by inversion of the in-situ SE data were parameterized from 0.75 to 4 eV using a constant real contribution ε_{1o}, four CP oscillators, and one broad background Tauc-Lorentz oscillator [6]. An Urbach tail was used for photon energies at and below the lowest CP energy $E_{CP,0}$. The oscillator parameters were expressed in terms of x by polynomial fitting. Fig. 4 shows the parametric results for the room temperature (ε_1, ε_2) spectra predicted for films with $x=[Ga]/\{[In]+[Ga]\}=0.05$, 0.15, 0.25, 0.35, and 0.45. This figure shows clear monotonic behavior, as indicated by the arrows, with increases in the CP energies with increasing x. For the Ga content of $x=0.30$, which is of greatest interest as it defines the optimum in solar cell performance, the CP resonance energies are 1.19, 1.42, 2.94, and 3.76 eV. The Tauc-Lorentz oscillator resonance energy is 6.23 eV, and the Tauc gap E_G is equated to the lowest CP energy $E_{CP,0}=1.19$ eV. For the film with Ga content of $x=0.30$, all parameters that define the (ε_1, ε_2) spectra are presented in Table 1. Table 2 presents the polynomial expressions that provide the parameters for a CIGS film with any value of $\Delta x=x-0.30$ for $0\le x<0.5$ with fixed $y=0.90\pm0.03$.

For chemical bath deposited CdS, the SE measurements were performed ex-situ over the photon energy range from 0.75 to 6.5 eV at a single angle of incidence of 65° [11]. The experimental (ψ, Δ) spectra were obtained with an acquisition of <10 s to minimize oxidation. These spectra are shown in Fig. 5 over the narrower spectral range of 0.95 to 4.1 eV for samples prepared with $x=[Cd]/[S]$ molar ratios of 0.2, 0.4, 0.6, 0.8, and 1.0 (points). The model for the structure applied both bulk and surface roughness layers, the latter with a variable void content. The model for the (ε_1, ε_2) spectra used a constant real contribution ε_{1o} fixed at unity and two CP oscillators for a parametric form over the depicted spectral range. Fig. 5 shows the best fit results obtained by least squares regression analysis with photon energy independent structural and optical parameters from the models. The confidence limits on the parameters of the second higher energy oscillator were found to be large due to the limited spectral range of analysis, up to ~4.1 eV. As a result, the simultaneously determined structural parameters were fixed, enabling inversion of the SE data to extract the (ε_1, ε_2) spectra for the five samples.

The (ε_1, ε_2) spectra of the CdS films obtained by inversion were then fit using multi-sample analysis with the same model for (ε_1, ε_2) applied to each sample; however, the parameters of the second CP oscillator were fixed to the same set of values for all five samples. This was done to minimize the number of free variables needed to determine the (ε_1, ε_2) spectra for the set of CdS films, but without affecting the quality of the fits and the accuracy of the spectra. The final parametric results following this procedure are shown in Fig. 6. Here one can observe that, with the increase in concentration ratio of Cd to S precursors, the bandgap as determined from the ex-situ SE analysis decreases from 2.50 eV to 2.38 eV. The latter band gap for $x=1.0$ is consistent with the result for wurtzite single crystal CdS [38]. The wider bandgap for the lower x values in the present study of CBD CdS may be due to the incorporation of oxygen in the CBD films [39]. The results for $x=1.0$ are characteristic of those of higher x values as well and have been used in the analysis of complete solar cells as described in Section 3.2. The full set of parameters defining the (ε_1, ε_2) spectra for the sample with $x=1.0$ is presented as the third data column in Table 1.

In this study, the optical properties of ZnO and ZnO:Al films deposited at different substrate temperatures were characterized using a variable angle spectroscopic ellipsometer [40,41] having a single channel (or wavelength-by-wavelength) rotating analyzer

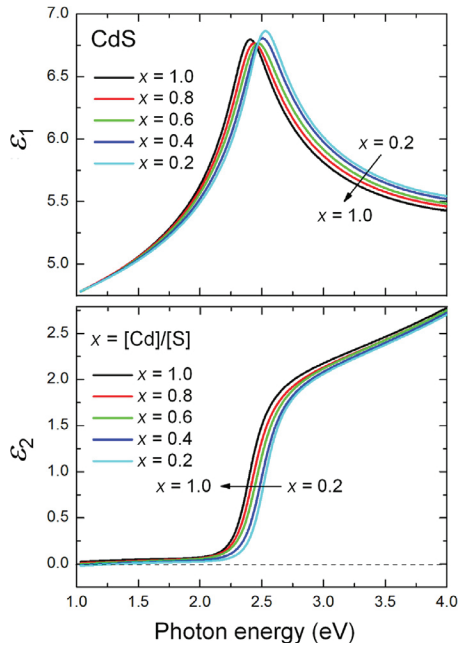

Fig. 6. Room temperature complex dielectric function spectra (ε_1, ε_2) for CdS films prepared by chemical bath deposition from different molar ratios $x=[Cd]/[S]$ of the precursors cadmium acetate and thiourea. The (ε_1, ε_2) spectra determined from ex-situ SE measurements are fit using a parametric expression describing an oscillator model with two critical points, one simulating the bandgap, as shown by the peak in ε_1 and the step in ε_2, and the other simulating the above bandgap transitions. The parameters defining the (ε_1, ε_2) spectra for the sample with $x=1.0$ are presented as the third data column in Table 1.

design (V-VASE, J. A. Woollam Co.). Measurements were performed at angles of incidence of 65°, 70°, and 75° over the photon energy range from 0.95 to 4.1 eV. This approach was used for the ZnO and ZnO:Al films since oxidation of the film surfaces during the ex-situ measurement was of less concern than for the Mo, CIGS, and CdS films. Representative experimental (ψ, Δ) spectra and best fit results for the ZnO films are shown in Fig. 7. For both ZnO and ZnO:Al films on thermally oxidized Si wafers, the structural model was the same, including variable thickness bulk and surface roughness layers with a variable void content in the surface roughness layer; however, the optical models for the materials differed.

For the undoped ZnO films, which show an excitonic feature at the bandgap energy [34], the dielectric function model applied here includes the constant real term ε_{1o}, a single Tauc-Lorentz oscillator, and two CP oscillators [11]. The constant ε_{1o} could be fixed at unity due to the use of three oscillators, and the Tauc gap E_G was equated to the lowest CP energy $E_{CP,0}$ to avoid absorption below $E_{CP,0}$ due to the Tauc-Lorentz oscillator. In the model, a possible Drude term and an Urbach tail are not necessary because the ZnO layer is thin in the solar cell structure, and any associated contributions to absorption below the ZnO bandgap are negligible. Multi-sample analysis was also performed for ZnO to assist in stabilizing the multi-angle fitting process. In this analysis, E_{TL} and Γ_{TL} values were equated for all samples, and the higher energy CP resonance energies $E_{CP,1}$ were equated, as well. Fig. 8 shows the final results for the (ε_1, ε_2) spectra of the ZnO. For these spectra, the bandgap does not depend on substrate temperature, remaining constant at 3.32 eV; however, the amplitude $A_{CP,0}$ of the dominant CP increases with increasing substrate temperature, suggesting an increase in the density of these films. For all solar cells, however, room temperature substrate temperature is employed to avoid exceeding the deposition temperature of the CdS. Thus, the 20 °C spectra in Fig. 8 are used in the EQE modeling of the solar cells. The fourth data column in Table 1 presents the photon energy

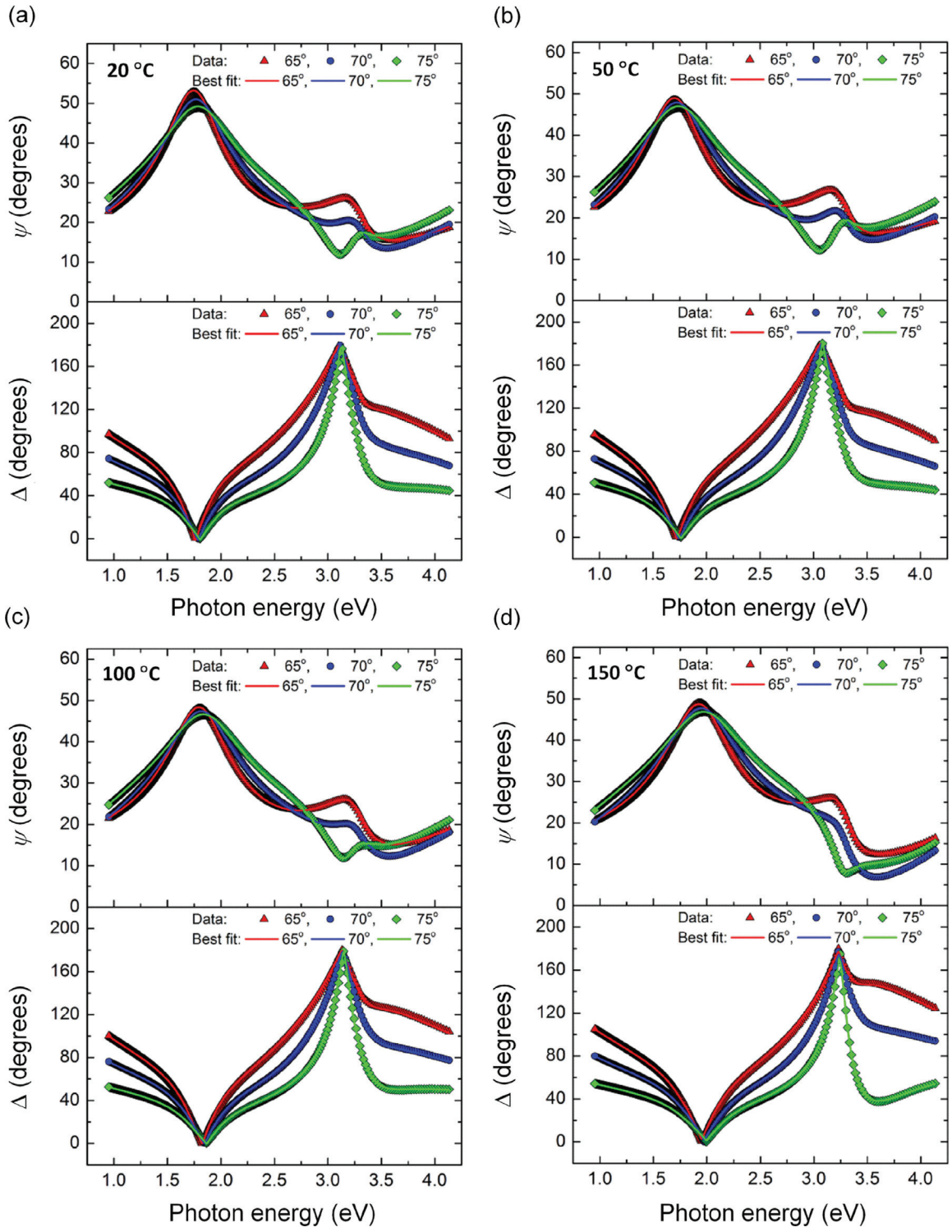

Fig. 7. Measured ex-situ SE data at room temperature for three angles of incidence, 65°, 70°, and 75° (symbols), along with best fit simulations (solid lines), obtained in studies of ZnO films deposited onto c-Si wafers with themal oxides using magnetron sputtering at substrate temperatures of (a) 20 °C, (b) 50 °C, (c) 100 °C, and (d) 150 °C.

independent parameters that describe the (ε_1, ε_2) spectra of the ZnO deposited at 20 °C.

For the ZnO:Al films, the model applied here to describe each pair of (ε_1, ε_2) spectra includes the constant real term ε_{1o}, a Drude term, a single Tauc-Lorentz oscillator, and a single CP oscillator [11]. As in the study of ZnO, the Tauc gap E_G is coupled to the band gap CP energy $E_{CP,0}$ for these films. By equating all Tauc-Lorentz oscillator resonance energies for the full set of ZnO:Al samples and doing the same for the broadening parameters, a multi-sample analysis of the four ZnO:Al complex dielectric functions enables improved stability of the fitting. Fig. 9 shows the final results for the best fit parametric (ε_1, ε_2) spectra. These results also suggest a monotonic increase in amplitude with substrate temperature attributed to a reduction in void content. In addition, the CP energy which defines the bandgap of the ZnO:Al increases continuously from 3.71 eV to 3.82 eV, a range that is much higher than the value

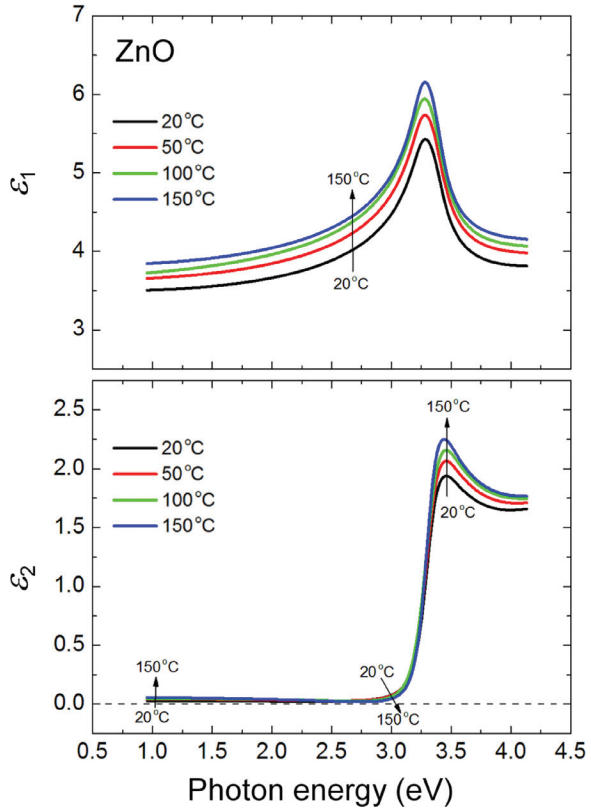

Fig. 8. Room temperature dielectric function spectra (ε_1, ε_2) for ZnO thin films deposited by magnetron sputtering at nominal substrate temperatures of 20 °C, 50 °C, 100 °C, and 150 °C. These results are based on analysis of ex-situ SE data of Fig. 7 and are determined from the best fit parametric expressions for (ε_1, ε_2). The expressions employ an oscillator model consisting of two critical points that describe the excitonic behavior at the bandgap as well as a high energy background Tauc-Lorentz oscillator to describe the effect of above-gap transitions. The parameters defining the (ε_1, ε_2) spectra for the sample deposited at 20 °C are presented as the fourth data column in Table 1.

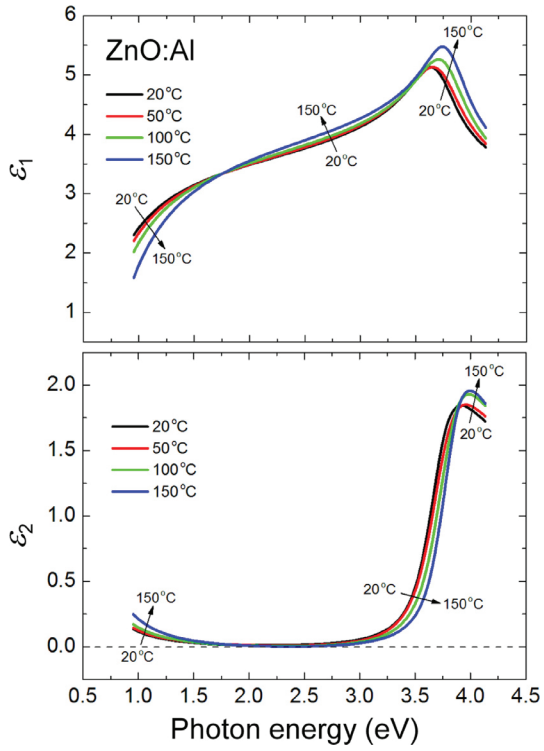

Fig. 9. Room temperature dielectric function spectra (ε_1, ε_2) determined from best fit parametric expressions for ZnO:Al thin films deposited by magnetron sputtering at nominal substrate temperatures of 20 °C, 50 °C, 100 °C, and 150 °C. The parametric expression for the (ε_1, ε_2) spectra includes a Drude contribution, a Tauc-Lorentz oscillator describing above bandgap transitions, and a critical point oscillator describing the bandgap transitions. The parameters defining the (ε_1, ε_2) spectra for the sample deposited at 20 °C are presented as the fifth data column in Table 1.

of 3.32 eV for undoped ZnO. The higher bandgap for ZnO:Al is due to the shift of the Fermi energy into the conduction band, i.e., the Burstein-Moss band filling effect [42,43]. The further increase in bandgap for ZnO:Al with increasing substrate temperature is likely to be caused by an increase in electron concentration. This effect is consistent with the more rapid decrease in $\varepsilon_1(E)$ with decreasing E in the near-infrared range and with the corresponding more rapid increase in $\varepsilon_2(E)$ as the substrate temperature increases. In fact, from the best fit Drude term one finds a decrease in ρ and an increase in τ with substrate temperature, which is consistent with the increase in carrier concentration and also an increase in crystalline grain size. As noted in the previous paragraph, the 20 °C deposition is used for solar cells and the corresponding spectra in Fig. 9 are used in the SE-EQE analysis in spite of these improvements with increasing substrate temperature. The fifth data column in Table 1, presenting the photon energy independent parameters that describe the (ε_1, ε_2) spectra of the ZnO:Al deposited at 20 °C, completes the parametric set of data for the CIGS solar cell without ARC. One observation that can be made for the CIGS, ZnO, and ZnO:Al parameters is the large width of the Tauc-Lorentz oscillator. This reflects the fact that this oscillator is used in the model to simulate the electronic transitions that are not associated with CPs, i.e., the electronic transitions between bands that are not parallel. As a result, the Tauc-Lorentz oscillator parameters lack a clear physical meaning in contrast to the CP parameters.

In this study, the room temperature optical properties of MgF_2, HfO_2, ZrO_2, TiO_2, SiO_2, and Al_2O_3 thin films were measured us-

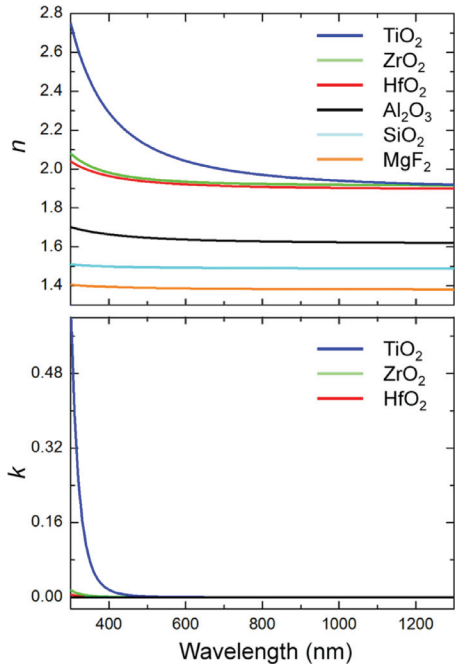

Fig. 10. Optical properties including index of refraction n and extinction coefficient k spectra at room temperature over the wavelength range from 300 to 1300 nm as deduced by ex-situ SE for MgF_2, HfO_2, ZrO_2, TiO_2, SiO_2, and Al_2O_3 anti-reflection coating materials. These spectra are obtained from analytical expressions including a Cauchy series in wavelength for the index of refraction and an exponentially decreasing function of wavelength for the extinction coefficient.

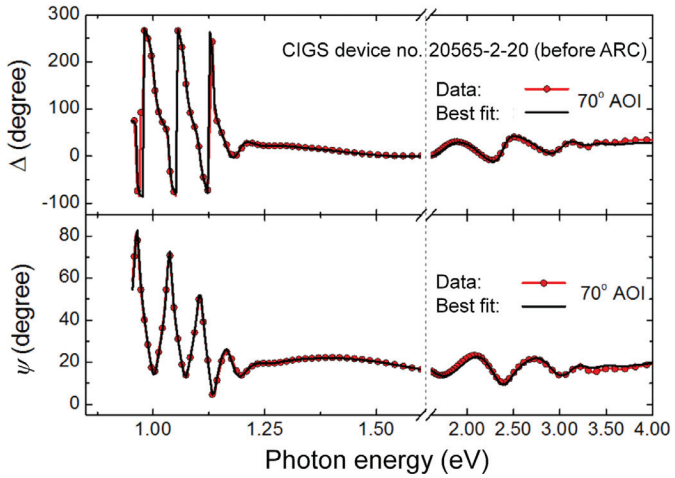

Fig. 11. Measured ex-situ SE spectra obtained at an angle of incidence of 70° and represented in terms of the ellipsometry angles (ψ, Δ) for a CIGS solar cell with a standard absorber layer of 2.2 μm thickness and with no ARC (symbols). Also shown is the simulation (solid lines) applying the best fit structural model and compositional profile shown in Fig. 12.

ing ex-situ variable angle SE and parameterized in order to establish a database of potential ARC materials for multilayer structures [11]. Substrates of c-Si with pre-determined oxide layer thicknesses were used for all depositions, including both electron beam evaporation and atomic layer deposition processes. The SE data were analyzed using an optical model incorporating bulk layer and surface roughness layer thicknesses. The thicknesses of the bulk layers of these films were in the range from 32 to 197 nm, and those of the surface roughness layers were in the range from 0.9 to 2.8 nm. Because of the very thin roughness layers, they are assumed to consist of 50/50 vol% bulk/voids. The (ε_1, ε_2) spectra were obtained applying point-by-point fitting in an analysis that also identifies the best fit values for the layer thicknesses. Parametric forms for these best fit spectra were then obtained using a model that includes a Cauchy series dispersion equation for the index of refraction with terms in E^{2m} ($m=0$, 1, 2), which derives from a binomial expansion in photon energy of the square-root of a single Sellmeier term [2,6]. An exponential absorption onset was used for the extinction coefficient for films that are absorbing in the near-ultraviolet range. The final results are shown in Fig. 10 for the six different materials; only the HfO_2, ZrO_2, and TiO_2 exhibit nonzero k values at the highest photon energies. Although the performances of bilayer ARCs of HfO_2 and MgF_2 have been simulated on a map in the plane of the two thicknesses, as shown in Section 3.3, only single layer ARCs of MgF_2 have been used on the fabricated solar cells. For the MgF_2 thin film of Fig. 10, the deduced index of refraction was found to be $n(E)=1.3800+(0.0015/\text{eV}^2)E^2$.

3.2. Spectroscopic ellipsometry analysis of solar cells

For complete CIGS solar cells in the substrate configuration, ex-situ SE was performed in reflection from the film side at a single location that avoids the collection grids on the device surface. The ex-situ SE data were acquired at a 70° angle of incidence over the photon energy range from 0.9 to 4.0 eV using a single-channel rotating-analyzer ellipsometer with an auto-retarder (V-VASE, J.A Woollam Co.) [11]. By utilizing the component layer (ε_1, ε_2) spectra as presented and discussed in the previous section, the SE data were analyzed by applying least squares regression. For the CIGS absorber layer, the optical property database consists of polynomial coefficients enabling calculation of the photon energy independent parameters defining the (ε_1, ε_2) spectra for CIGS material of any Ga content x [31]. Through the least squares regression analysis with all photon energy independent parameters, the multilayer structural/compositional information for the solar cell was determined non-invasively [11,20,22]. For the CIGS solar cell, the following information was determined: (i) the thickness of each layer, (ii) a void fraction in each layer as needed, (iii) the thickness and composition of each interface roughness layer and the surface roughness layer, and (iv) the Ga compositional profile consisting of two linear segments within the CIGS absorber layer. The parameters in the model assumed for the Ga profile include values of Ga composition x at the junction x_{HF}, at the minimum within the CIGS layer x_L, and at the back contact x_{HB}, as well as the depth d_L from the junction at which the minimum in x occurs. The CIGS components in the effective media that describe the Mo/CIGS and CIGS/CdS interface roughness layers are assumed to have Ga contents of x_{HB} and x_{HF}, respectively, i.e., the same as those at the back and front of the bulk CIGS layer.

Ex-situ SE data in the form of (ψ, Δ) are shown in Fig. 11 (points) for a CIGS solar cell having the standard absorber layer thickness of 2.2 μm and no ARC [11,20,22]. Thus, these SE data were measured non-invasively prior to ARC deposition. The results in Fig. 12 were determined using least-squares regression analysis as the best fit (solid lines) to the data of Fig. 11. Fig. 12(a) shows the multilayer model that describes the CIGS solar cell, including the best fit structural and compositional parameters associated with the component layers. For each layer of the stack, one can calculate the effective thickness, meaning the volume of the given material per unit area. This is obtained as the product of the layer thickness and the volume fraction of the material summed over all layers that include the material. For example, from the results in Fig. 12(a), the effective thickness of the CIGS absorber is calculated as $(19.9\,\text{nm})(0.180)+(2177.7\,\text{nm})+(59.1\,\text{nm})(0.775)=2227.1\,\text{nm}$, in good agreement with the intended value of 2.2 μm. The CdS, ZnO, and ZnO:Al effective thicknesses in Fig. 12(a) are calculated as 83.2 nm, 89.6 nm, and 238.0 nm, respectively. It should be noted that $MoSe_2$ is not explicitly included at the Mo/CIGS interface in the optical model of the solar cell in Fig. 12(a). This is not to imply that such a phase does not exist in the sample, but may instead suggest that the effective medium mixture of Mo and CIGS with variable composition is sufficient to account for the Mo/CIGS interface optical response. In fact, with the Mo/CIGS interface characteristics used in the model, finer details of the cell structure can be deduced by SE such as the Ga profile as will be discussed next.

Fig. 12(b) depicts the SE-determined Ga profile for the CIGS absorber layer obtained in the same fitting procedure, including the four free parameters, x_{HF}, x_L, x_{HB}, and d_L. A secondary ion mass spectrometry (SIMS) depth profile was also measured for this sample using a single calibration parameter to scale the composition [22]. The resulting profile is given in Fig. 12(b) for comparison with the compositional profile deduced by SE. The shapes of the SE and SIMS profiles are found to be in good agreement, supporting the validity of the SE method for profile determination. Good agreement has been obtained as well in a comparison of depth profiles deduced by Auger electron spectroscopy (AES) and by SE. The AES-SE comparison was made in a study of a 0.36 μm CIGS layer deposited by three-stage co-evaporation directly on soda lime glass [31].

For the same solar cell of Figs. 11 and 12 with the standard 2.2 μm absorber, an additional ex-situ SE measurement was performed after the ARC deposition [11]. By ensuring that the same spot between the grids was measured on the device before and after ARC deposition, a multilayer model could be established for data analysis using fixed parameters for all layers with the exception of those incorporating the MgF_2 ARC material. Thus, the variable parameters include the layer thicknesses of the ZnO:Al/MgF_2

(a)

CIGS device no. 20565-2-20 (before ARC)

layer (composition, properties)	thickness
surface roughness (f_v = 30.6%)	34.29 ± 2.06 nm
ZnO:Al (f_v = 2.9%)	111.97 ± 2.79 nm
i-ZnO / ZnO:Al (f_{ZnO} = 21.8%, f_v = 2.9%)	140.08 ± 2.30 nm
i-ZnO (f_v = 0.0%)	36.23 ± 1.67 nm
CdS / i-ZnO (f_{CdS} = 48.6%, f_v = 0.0%)	44.47 ± 1.78 nm
CdS (f_v = 0.0%)	48.67 ± 1.15 nm
CIGS / CdS (f_{CIGS} = 77.5%, f_v = 0.7%)	59.12 ± 1.49 nm
CIGS (graded layer, f_v = 0.0%) (x_{HF} = 0.304 ± 0.011, x_L = 0.182 ± 0.036, x_{HB} = 0.469 ± 0.032)	2177.73 ± 2.28 nm
Mo / CIGS (f_{Mo} = 82.0%)	19.89 ± 2.31 nm
Mo (opaque)	

(b)

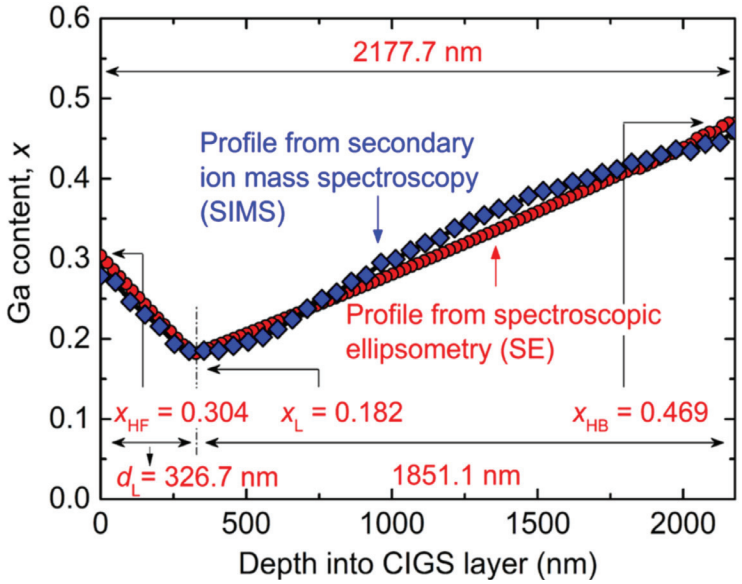

Fig. 12. (a) Multilayer structure of a CIGS solar cell incorporating an absorber layer with a standard 2.2 μm thickness and having no ARC. (b) A comparison of the Ga profiles in the absorber of the same solar cell as deduced from SE and SIMS analyses. The SE results in (a) and (b) were obtained from analysis of the ex-situ SE data in Fig. 11.

interface, the MgF_2 bulk, and the MgF_2 surface roughness. Compositions for these layers were determined as well, allowing for the possibility of density deficits, i.e., void volume fractions, in each of the layers applying two and three-component EMAs. This analysis yields an effective thickness of the two-layer MgF_2 bulk/roughness structure of 91 nm, close to the intended value of 94 nm. The intended value is based on the simulation presented in Section 3.3, a value optimized for J_{SC} of the solar cell.

Ex-situ SE (ψ, Δ) spectra are shown in Fig. 13 (points) for the CIGS solar cell with the thin absorber layer with intended thickness of 0.5 μm [11]. These measurements were performed before ARC deposition on the ZnO:Al/grids surface of the solar cell, avoiding the grids. The results given in Fig. 13 as the solid lines are the best fit results determined by least squares regression analysis of the data. Fig. 14(a) shows the CIGS multilayer solar cell stack applied in the analysis and the best fit structural and compositional parameters. These results are presented along with Fig. 14(b), a depiction of the SE-determined Ga profile for the CIGS absorber layer as obtained in the same fitting procedure. The schematic of Fig. 14(a) shows effective thicknesses for the CIGS, CdS, ZnO, and ZnO:Al layers of 533.5 nm, 69.0 nm, 95.6 nm, and 250.0 nm, respectively.

Interesting differences can be noted between the results for the thin solar cell in Fig. 14 and the standard thickness cell of Fig. 12. First, it should be noted that for the cell with the thin absorber, the value of x when averaged through the absorber profile is $<x>=0.255$, lower than $<x>=0.313$ for the cell with the 2.2 μm thick absorber. This reduction is intentional since for thin

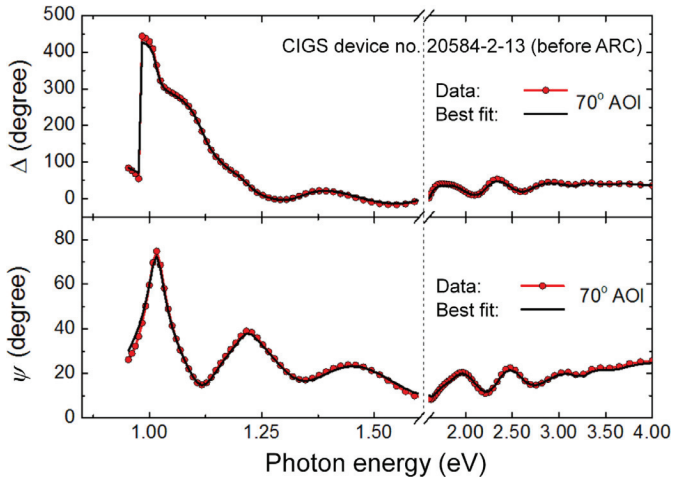

Fig. 13. Measured ex-situ SE data obtained at an angle of incidence of 70° (symbols) and represented in terms of the ellipsometry angles (ψ, Δ) for a CIGS solar cell with a 0.5 μm thick absorber layer and with no ARC. Also shown is the best fit simulation (solid lines) applying the best fit structural model and compositional profile shown in Fig. 14.

cells, open-circuit voltage (V_{OC}) decreases weakly whereas J_{SC} increases strongly with decreasing x from $x = 0.30$. Thus for a cell with a thin absorber layer, it is beneficial to trade-off V_{OC} for J_{SC} in order to maximize efficiency [20,31]. Another interesting feature is that, although the Mo/CIGS interface layers arising predominantly from the roughness on the Mo surface are similar in thickness, 20–21 nm, for the two devices in Figs. 12 and 14, the CIGS/CdS interface layer is thinner for the cell with the thinner absorber, 35 nm, versus that of the standard absorber, 59 nm. This behavior is an indication that the roughness on the CIGS surface increases with increasing thickness, leading to a smoother heterojunction interface for thin absorbers, an effect noted in real time SE studies [44]. A smoother such interface enables thinning of the CdS without shunting. This accounts for the lower CdS effective thickness of 69 nm for the optimized cell with the thinner absorber layer, compared with effective thicknesses of 83 nm for the optimized cell with the standard absorber. In spite of the smoother CIGS/CdS interface for the 0.5 μm absorber, the CdS/ZnO interface layer is similar in thickness for cells with the 0.5 μm and standard absorbers, 47 and 44 nm, respectively. This suggests that the evolving roughness after the CdS deposition is controlled by the CdS, at least for the cell with the thin absorber.

3.3. External quantum efficiency simulations

In order to better understand current collection and losses in a CIGS solar cell structure, optical simulation is applied using the results of the SE analysis of the cell as inputs, starting with the cell of Fig. 12 having a standard thickness absorber [11,22]. Under the assumption of ideal collection of photo-generated carriers, i.e., no electronic losses, a normal incidence EQE spectrum can be predicted simply by summing the spectra describing the fractions of absorbed photons for the active component layers of the CIGS solar cell. It should be noted that the time average of the power dissipated per volume from the optical field $\mathbf{E}_j(z)$ at position z in layer j is given by [14,45]

$$Q_j(z) = (1/2)\,\omega\,\varepsilon_0\varepsilon_{2j}(z)\left|\mathbf{E}_j(z)\right|^2, \qquad (11)$$

where ω is the optical frequency and $\varepsilon_{2j}(z)$ is the imaginary part of the dielectric function at position z in layer j. This expression accounts for the possibility of an optically graded layer characterized by $\varepsilon_{2j}(z)$, as in the case of the CIGS absorber. Profiles of Q_j versus depth z within the layers and versus wavelength for the CIGS solar cell have been presented previously [21]. One can numerically integrate this function over z for layer j to obtain the power dissipation per area within the entire layer. Here, only the results from integrations of Eq. (11) are presented as these can be compared directly to measured EQE results once the active layers of the device are selected.

In the simulation, the CIGS/CdS interface and CIGS bulk layers are considered to be the active layers. In Fig. 15(a), these photon absorbance spectra are presented based on simulations for the CIGS solar cell of Fig. 12 with the standard 2.2 μm absorber and no ARC. The simulated spectra for these active layer components are summed to represent the total predicted EQE response in Fig. 15(a). In Fig. 15(b), the simulated EQE spectrum of Fig. 15(a) from the SE analysis is compared to the measured spectrum. Excellent agreement between the two spectra is found, including agreement in the simulated and experimental J_{SC} values [$J_{SC}(\text{sim}) = J_{SC}(\text{exp}) = 34.2\ \text{mA/cm}^2$]. These agreements demonstrate that the active layers in this CIGS solar cell are indeed the CIGS/CdS interface layer and the CIGS bulk layer. It is assumed that electrons and holes generated by light absorbed within the CIGS component of the Mo/CIGS interface roughness layer are not collected, as the trapping of electrons followed by recombination is likely to occur here. The assumption is supported by the results for thin cells which are more sensitive to this collection loss due to the larger effective thickness of CIGS contained in the Mo/CIGS interface layer relative to the total CIGS effective thickness.

These results are important for the following reasons. First, the results suggest that the optical model used to evaluate collection is accurate, and thus it can be used further to evaluate optical and electronic losses. As a demonstration, the photon absorbance spectra are presented in Fig. 15(c) calculated for each component layer of the solar cell of Fig. 12 having the 2.2 μm absorber layer and no ARC. The photon absorbance within the opaque Mo back contact is also included in Fig. 15(c), and the difference between unity and the absorbance sum including all layers provides the fraction of photons reflected from the cell. Second, because J_{SC} can be calculated directly from the EQE spectrum, it can be used as the single key output parameter from the simulation for use in optimizing device design. Thus, the method established here also allows investigation of the effects of component bulk layer and interface/surface roughness layer thicknesses, as well as composition profile, on the attainable J_{SC}, enabling further directions for improvement of the solar cell structure by optical means. A simple example of this approach is described next.

For a demonstration of the design capability associated with an accurate optical model of the cell, a MgF_2 ARC was deposited on the CIGS cell of Figs. 11, 12, and 15. The intended thickness was determined on the basis of an optimized simulation as shown in Fig. 16 [11]. In fact, the optimization was performed assuming a two layer stack of HfO_2/MgF_2. In this optimization, a map of J_{SC} gain in the plane defined by the HfO_2 and MgF_2 ARC layer thicknesses is generated first through simulation to identify an optimum bilayer. In the simulation, it is assumed that the HfO_2 fills the modulations in the ZnO:Al surface roughness (or the MgF_2 fills these modulation when the HfO_2 thickness vanishes), but that the bilayer interface and surface are smooth. Based on these assumptions, a maximum gain of 2.1 mA/cm^2 is identified for a vanishingly small HfO_2 thickness and for a MgF_2 bulk layer thickness of 94 nm as indicated in Fig. 16.

As a result of the optimization shown in Fig. 16, an intended MgF_2 effective thickness of 94 nm for the bulk/roughness layers was deposited on the solar cell of Figs. 11, 12, and 15 and measured by SE. The SE measurement results of the cell with the ARC reveal a MgF_2 effective thickness of 91 nm associated with the bulk/roughness layers in the model as described previously.

(a)

CIGS device no. 20584-2-13 (before ARC)

layer (composition, properties)	thickness
surface roughness (f_v = 35.9%)	36.93 ± 2.72 nm
ZnO:Al (f_v = 2.8%)	113.14 ± 2.46 nm
i-ZnO / ZnO:Al (f_{ZnO} = 20.9%, f_v = 2.8%)	152.17 ± 2.53 nm
i-ZnO (f_v = 0.0%)	39.17 ± 1.75 nm
CdS / i-ZnO (f_{CdS} = 47.4%, f_v = 0.0%)	46.81 ± 1.84 nm
CdS (f_v = 0.0%)	36.04 ± 1.59 nm
CIGS / CdS (f_{CIGS} = 68.3%, f_v = 0.6%)	34.52 ± 1.37 nm
CIGS (graded layer, f_v = 0.0%) (x_{HF} = 0.269 ± 0.015, x_L = 0.208 ± 0.034, x_{HB} = 0.307 ± 0.032)	504.81 ± 1.63 nm
Mo / CIGS (f_{Mo} = 80.6%)	21.39 ± 1.96 nm
Mo (opaque)	

(b)

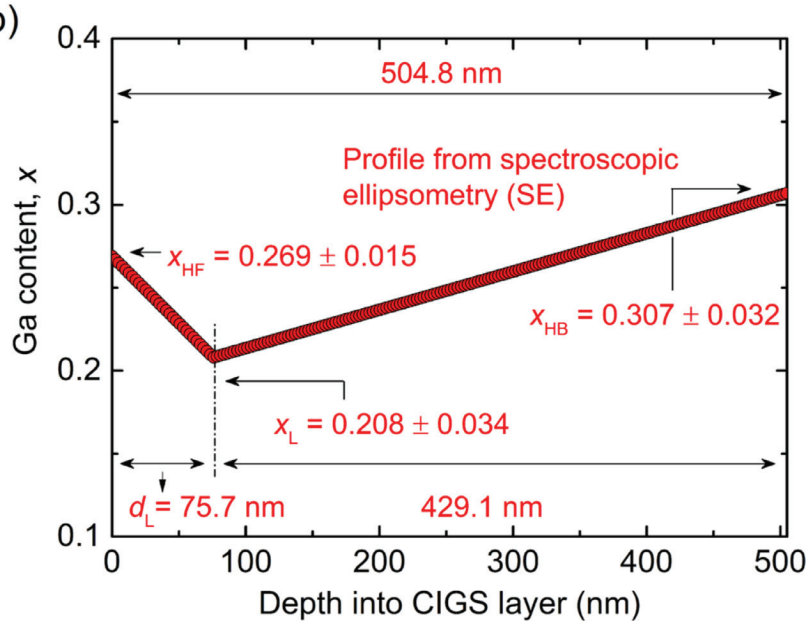

Fig. 14. (a) Multilayer structure of a CIGS solar cell incorporating an absorber layer having a 0.5 μm thickness and no ARC, and (b) Ga profile in the absorber layer of the same solar cell. These results were deduced from the ex-situ SE analysis of Fig. 13.

This effective thickness excludes the interface roughness contribution, which is not included in the thicknesses of Fig. 16, as well. Thus, the measured value is reasonably close to the intended value of 94 nm. Under the assumption of ideal collection of photo-generated carriers, i.e., no electronic losses, the EQE spectrum can be simulated optically for the standard CIGS cell incorporating the ARC. This is achieved by applying the SE determined model and best fit results to obtain the optical spectra for photon absorption within the two active component layers and then by summing these spectra [11]. In Fig. 17(a), the simulated absorption spectra within the active layers, the CIGS/CdS interface and CIGS bulk, are displayed and the sum is also given that represents the net simulated EQE response. In Fig. 17(b), the predicted EQE spectrum from the SE analysis of this standard CIGS cell with the ARC is compared to the measured spectrum. An experimental J_{SC} increase of 2.1 mA/cm^2 is recorded in the measurement, yielding $J_{SC}(\text{sim}) = J_{SC}(\text{exp}) = 35.9$ mA/cm^2. Thus, the measured improvement with the ARC is in agreement with the prediction and demonstrates the success of both the simulation and the ARC deposition. The resulting simulated photon absorbance spectra for all the layers within the multilayer structure, along with the fraction of photons reflected, are shown in Fig. 17(c) for the CIGS cell of Figs. 11, 12, and 15 with the incorporated ARC.

Next, the focus is on EQE simulations for the solar cell of Figs. 13 and 14 with the thinner CIGS absorber layer, having an intended thickness of 0.5 μm [11,20]. In Fig. 18(a), the photon absorbance spectra within the CIGS/CdS interface and CIGS bulk layers are simulated on the basis of the SE model of Fig. 14 for this cell. The two spectra are summed to generate the net EQE response under the assumption of 100% photo-generated carrier collection in the two active layers. In Fig. 18(b), the predicted EQE spectrum from the SE analysis with the assumption of ideal

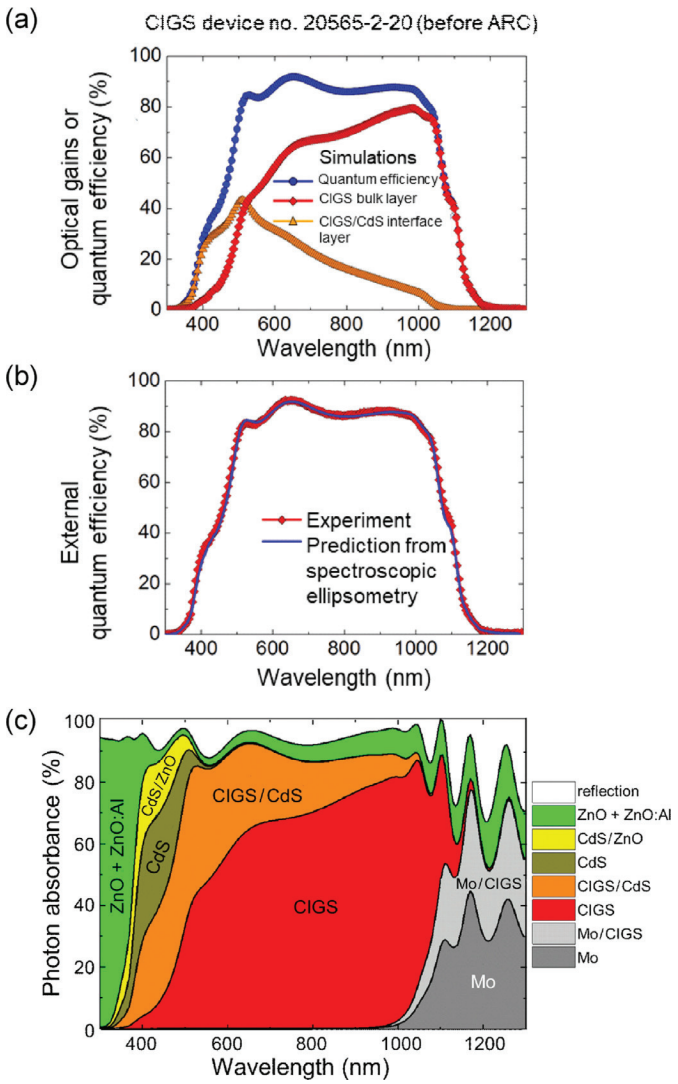

Fig. 15. (a) Simulated percentages of photons absorbed versus wavelength (or photon absorbance spectra) for the two active layers, including the CIGS/CdS interface and CIGS bulk layers, for the CIGS solar cell of Figs. 11 and 12 having a standard 2.2 μm thick absorber layer and no ARC. (b) A comparison of the measured and simulated EQE spectra is shown. The optical simulation assumes 100% charge carrier collection from the two active layer components. (c) Simulated photon absorbance spectra within the component layers are presented for the cell of (a) and (b). In (c), the deficit of the sum from 100% provides the reflectance of the solar cell. The simulations are based on the ex-situ SE analysis of the solar cell with no free parameters.

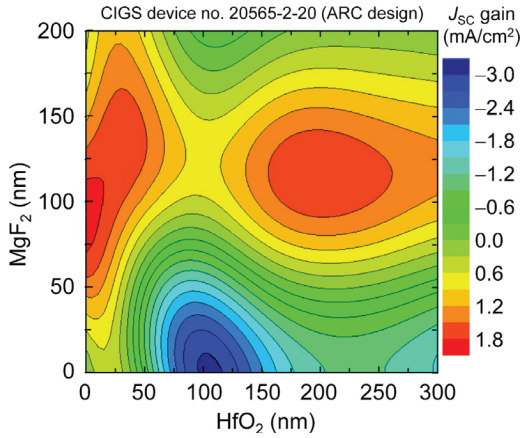

Fig. 16. Thickness optimization of a two-layer HfO_2/MgF_2 anti-reflection coating (ARC) in simulations using the underlying structure of the CIGS solar cell of Fig. 12 deduced as shown in Fig. 11. The simulations are based on the assumption of 100% photo-generated charge carrier collection from the active components including the CIGS/CdS interface and the CIGS bulk layers.

collection from the two active layers is compared to the measured spectrum. Reasonable overall agreement between the EQE spectra is observed in Fig. 18(b); however, in contrast to the results for the cell with the standard thickness absorber, the simulated EQE spectrum for the cell with the thin absorber consistently exceeds the measured one, starting at a wavelength of 500 nm and extending to 1100 nm. From the simulated EQE spectrum, a J_{SC} value of 32.8 mA/cm^2 is calculated whereas from the measured one, a J_{SC} value of 31.9 mA/cm^2 is determined.

The deficit between the two values of 0.9 mA/cm^2 suggests the presence of carrier recombination losses not only within the Mo/CIGS interface layer, but also within one or both of the active components, such that some photo-generated carriers exhibit collection probabilities that are less than 100% [11,20]. The absorbances for photons within each of the component layers of the CIGS solar cell with the intended 0.5 μm absorber are presented in Fig. 18(c), which also includes the absorbance within the opaque Mo back contact. Because no photons are transmitted through the back contact Mo, the difference between unity and the absorbance sum provides the reflectance of the cell. The discrepancy between the simulated and measured EQE in Fig. 18(b) can be understood by introducing a collection probability profile within the CIGS bulk layer to account for recombination losses [11,20]. The probability profile shown in Fig. 19(a) leads to a reduction in the discrepancy between the simulation and measured EQE as shown in Fig. 19(b). Thus, the losses that account for the discrepancy appear to occur in the CIGS bulk layer nearest the Mo back contact. It is not expected that $MoSe_2$ accounts for the increased losses since the Mo/CIGS interface layer incorporates any interaction between the CIGS and Mo, and the absence of collection from this layer appears to occur irrespective of the CIGS thickness [11,20].

It is also of interest to consider an ARC for the solar cell of Figs. 13, 14, and 18 with the absorber layer thickness of 0.5 μm [11]. For this cell, thickness optimization of the MgF_2 ARC is performed in one case assuming 100% charge carrier collection from the active layer components and in a second case assuming reduced collection from the CIGS bulk layer. The reduced collection is described by the collection probability profile in Fig. 19(a) for the solar cell, as described in the previous paragraph. It should be noted that the structural parameters, the $\varepsilon(E)$ spectra as appropriate, and the compositional profile applied in these simulations were obtained from the SE measurement and analysis results of Fig. 14. For simulations performed with both 100% collection in the active layers and reduced collection according to the profile of Fig. 19(a), maxima in J_{SC} occur at the same MgF_2 bulk layer thickness of 92 nm (assuming that MgF_2 upon deposition also fills the surface roughness in the ZnO:Al layer). The simulations also suggest that an enhancement in J_{SC} of 1.9 mA/cm^2 is possible via the ARC for this cell with the 0.5 μm thick absorber. Implementation of the ARC also yielded an experimental J_{SC} improvement precisely consistent with the gain predicted from the optical simulation, as described in detail in Ref. [11]. Thus for a solar cell with a reduced thickness absorber, the optical model for the solar cell deduced by SE predicts correctly the performance gain from ARC deposition.

CIGS solar cells with intended 0.7, 0.35, and 0.3 μm absorbers were also fabricated by three-stage co-evaporation and studied using ex-situ SE to deduce their multilayer structures and Ga compositional profiles [11,20]. Simulated EQE spectra for these additional cells were generated under the assumption of 100% photo-generated charge carrier collection from the two active layers. For

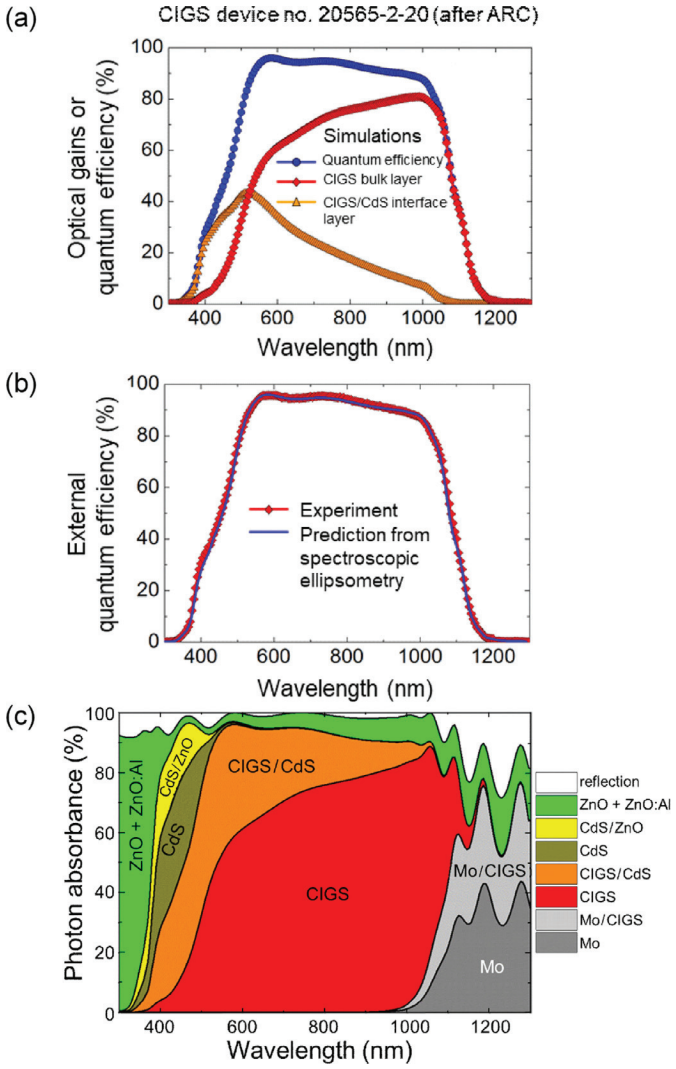

Fig. 17. (a) The simulated percentages of photons absorbed versus wavelength (or photon absorbance spectra) for the two active layers, including the CIGS/CdS interface and CIGS bulk layers, for the CIGS solar cell of Figs. 11 and 12 having a standard 2.2 μm thick absorber layer and an ARC. (b) A comparison of the measured and simulated EQE spectra is shown. The optical simulation assumes 100% charge carrier collection from the two active layer components. (c) Simulated photon absorbance spectra within the component layers are presented for the cell of (a) and (b). In (c), the deficit of the sum from 100% provides the reflectance of the solar cell. The simulations are based on the ex-situ SE analysis of the solar cell with no free parameters.

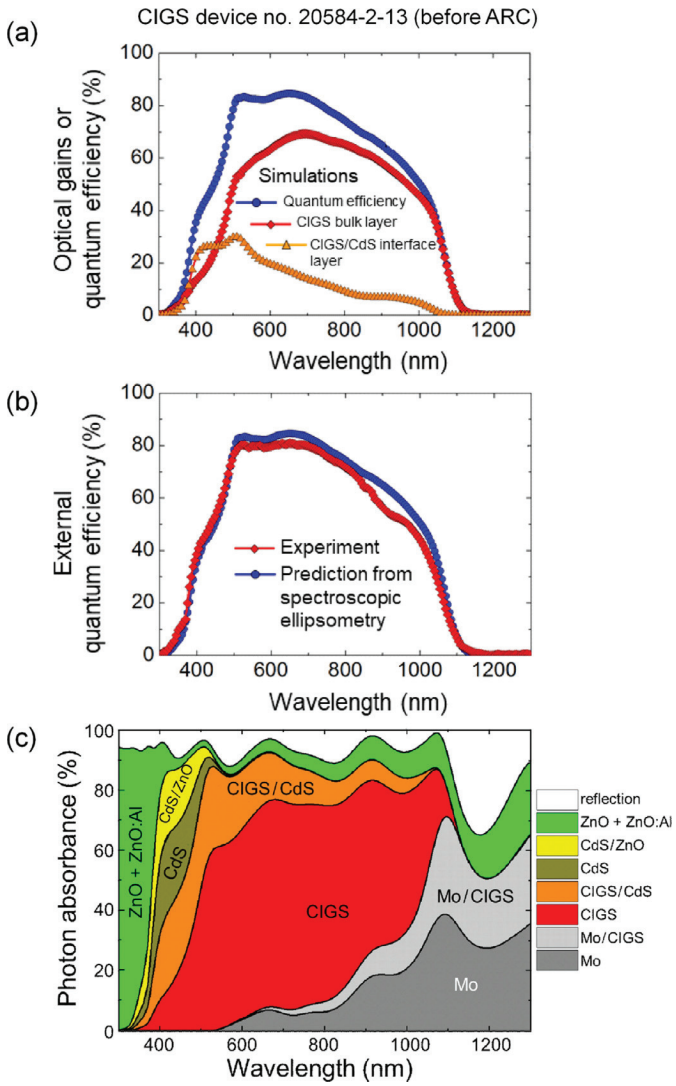

Fig. 18. (a) The simulated percentages of photons absorbed (or photon absorbance spectra) for the two active layers, including the CIGS/CdS interface and CIGS bulk layers, for the CIGS solar cell of Figs. 13 and 14 having a 0.5 μm thick absorber layer and no ARC. (b) A comparison of the measured and simulated EQE spectra is presented. The optical simulation assumes 100% charge carrier collection from the active layer components. (c) Simulated photon absorbance spectra within the component layers are presented for the cell of (a) and (b). The deficit of the sum from 100% provides the reflectance of the solar cell. The simulations are based on the ex-situ SE analysis of the solar cell with no free parameters.

these additional CIGS solar cells with thin absorbers, the simulated EQE values across the spectra were higher than those measured, and behavior similar to that shown in Fig. 18(b) was found for each cell. The difference between the simulated and measured EQE spectra could be understood in each case by introducing a carrier collection probability profile similar to that of Fig. 19(a) to represent the actual carrier collection from different depths within the CIGS bulk layer. For the cells with 0.7, 0.35, and 0.3 μm absorbers, the carrier collection was also found to be reduced near the back contact as was observed for the cell with the 0.5 μm absorber. In fact, as the absorber thickness decreases, these carrier recombination losses increase monotonically.

In Fig. 20(a), the optically simulated J_{SC} values assuming 100% photo-generated charge carrier collection from the two active layers are plotted versus the CIGS bulk layer thickness and compared for the solar cells without and with ARCs investigated in this study. Also in Fig. 20(a), the J_{SC} values measured for the cells without ARCs are compared to the corresponding simulated values. The difference between the simulated and measured values for the cells without ARCs is shown as a function of CIGS bulk layer thickness in Fig. 20(b). This difference is attributed to the carrier recombination losses which increase from undetectable values for a high performance solar cell incorporating a standard 2.2 μm thickness absorber layer to 5.4 mA/cm^2 for a cell incorporating an ultra-thin absorber 0.3 μm in thickness. Based on the overall results, it is found that for the cells with absorber layer thicknesses in the studied range of 0.3 to 0.7 μm, poor collection occurs consistently from the 0.15 μm region close to the back contact. Such a region may also exist to a certain extent for the cells with standard 2.2 μm thick absorbers; however, in contrast to cells with thin absorbers, the electrons and holes generated in this region are a relatively small fraction of the total generated in the standard thickness absorber.

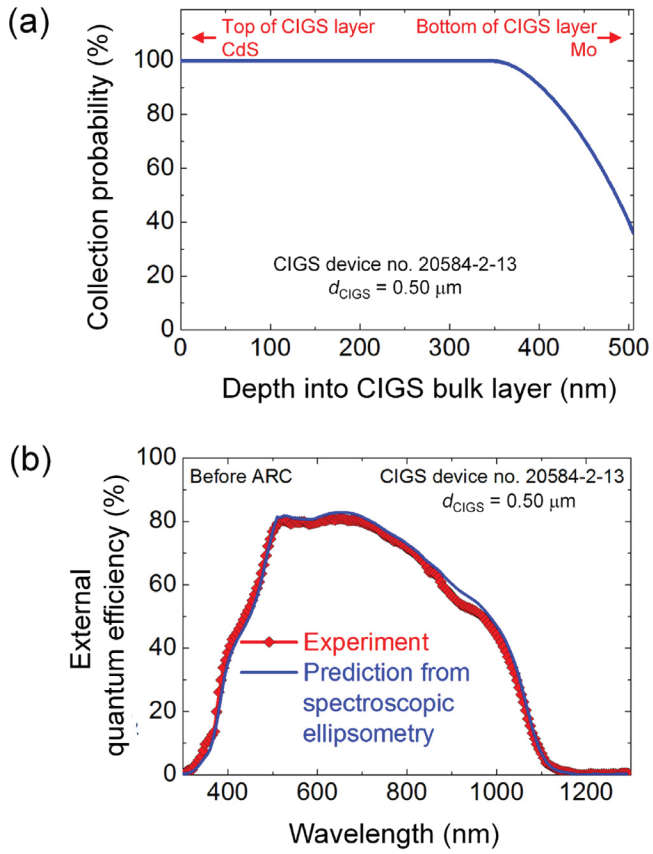

Fig. 19. (a) Collection probability profile used in an optical simulation that accounts for recombination losses of photo-generated charge carriers within the bulk component of the 0.5 μm CIGS absorber layer nearest the interface to the Mo back contact. (b) The EQE spectrum predicted optically for a CIGS solar cell with a 0.5 μm absorber layer and with no ARC, assuming 100% collection probability from the CIGS/CdS interface layer and a reduced carrier collection probability profile from the CIGS bulk layer according to (a). The measured EQE spectrum in (b) is also presented for comparison with the simulation.

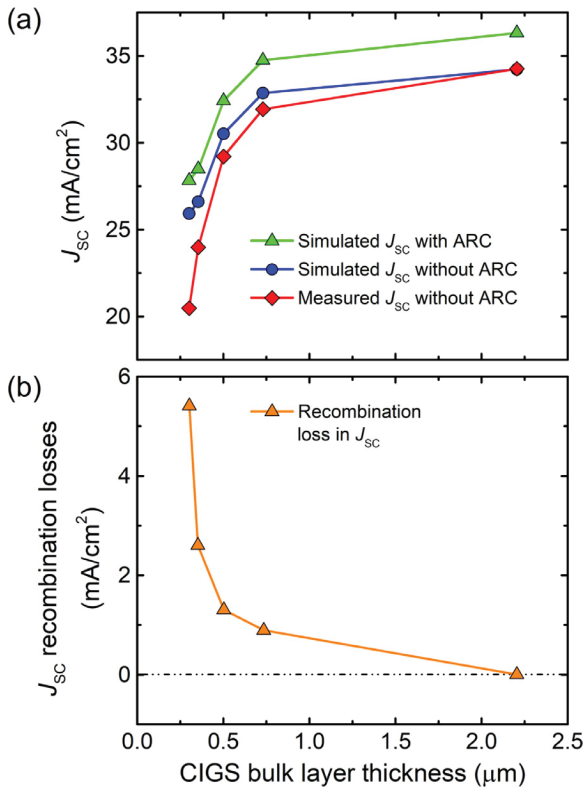

Fig. 20. (a) Measured and simulated short-circuit current density J_{SC}, the latter applying an optical model based on the assumption of 100% charge carrier collection within the CIGS/CdS interface and CIGS bulk layers. These results are plotted versus the CIGS bulk layer thickness for solar cells with standard 2.2 μm and thin CIGS absorbers and without ARCs. Also included are the results of the simulations for same set of solar cells but with the optimized ARCs. (b) Losses in J_{SC} due to recombination near the back contact are plotted vs. the CIGS bulk layer thickness corresponding to the results in (a) for the cells without ARCs.

4. Conclusions

The results presented in this article illustrate the development of an optical metrology based on spectroscopic ellipsometry (SE) for generating accurate inputs that enable external quantum efficiency (EQE) simulations of solar cells for direct comparison with EQE measurements. The goal is to understand in greater depth the origins of the optical performance limitations for thin film photovoltaics technologies through analyses of optical collection by the active components of the device, as well as analyses of optical and electronic losses via reflection, inactive layer absorbance, and active layer recombination. In this study, $CuIn_{1-x}Ga_xSe_2$ (CIGS) solar cells with both standard thickness and thin absorbers were characterized using SE to deduce the multilayer solar cell inputs necessary for EQE simulation. CIGS is more challenging than other thin films due to the need to extract the Ga profile throughout the absorber layer for a suitable structural/compositional model that generates accurate EQE inputs.

The first step in the development of the SE analysis and EQE simulation capabilities is to establish a database of spectra in the complex dielectric function $(\varepsilon_1, \varepsilon_2)$ for the solar cell components, preferably expressed as analytical formulas with photon energy independent parameters. For CIGS, this foundational work on optical model development must be performed on Mo, $CuIn_{1-x}Ga_xSe_2$ versus x, CdS, ZnO, ZnO:Al, and MgF_2. Although the $(\varepsilon_1, \varepsilon_2)$ spectra of these thin film materials have been studied widely, the resulting spectra depend on the deposition conditions, and possibly the layer thickness and substrate as well. Thus, analytical formulas for the $(\varepsilon_1, \varepsilon_2)$ spectra with variable photon energy independent parameters can be used to address these dependences. Given the availability of sufficient optical models for the components, the second step in the development of the capabilities is to establish a structural/compositional model for the complete solar cell that can be used to analyze the ex-situ SE data for the solar cell. This model includes bulk, interface roughness, and surface roughness layers and the associated compositional parameters, as well as the parameters that describe the Ga profile in the CIGS absorber layer and possibly other optical parameters.

Applying inputs from the SE analysis results, derived from both optical and structural/compositional models of materials and devices, EQE spectra have been simulated under the assumption of complete photo-generated charge carrier collection in the CIGS-containing active layers. These active layers include the CIGS bulk layer and the CIGS/CdS interface roughness layer. For cells with standard thickness absorbers, excellent agreement between simulated and measured EQE is obtained based on this assumption. This observation provides support for the validity of the models used in the ex-situ SE analysis as well as the final results of that analysis. For a set of four cells with thin absorbers from 0.3 to 0.7 μm in thickness, however, the EQE spectra simulated under the assumption of 100% collection from the active layers exceed the measured spectra. This indicates the presence of charge carrier recombination losses in the active layers associated with thin absorbers. By introducing into the simulation a carrier collection probability

profile for the CIGS bulk layer such that carrier collection is reduced near the back contact, much closer agreement between the simulated and measured EQE is observed for the cells with the thin absorbers. As a result, the magnitude and origin of carrier collection losses via recombination can be determined. In fact, as the absorber thickness decreases, these carrier recombination losses account for a strongly increasing fraction from the maximum possible current.

In addition to the single spot ex-situ SE capability demonstrated in this article, the SE metrology can be applied as well in the future to generate maps of film multilayer structural parameters, compositional profile parameters, and short-circuit current density predictions [46]. The ex-situ mapping SE capability is made possible by the high measurement speed of <1 s per (ψ, Δ) spectra provided by the multichannel ellipsometer which exploits one dimensional array detectors. The mapping speed can be increased further in the future through two-dimensional array detectors which exploit one array index to image the solar cell structure along a line, reserving the second index for spectroscopy [47]. Then two dimensional spatial mapping is possible by the assembly of a series of line images. Through such future directions, multichannel SE may be enhanced as a more powerful metrology for the production line environment.

Acknowledgments

This article is based upon research supported by the Department of Energy and the National Science Foundation (NSF) under the F-PACE Program, Award Number DE-EE0005400. Preparation of this article was supported by NSF Award EECS-1665172. The authors acknowledge the assistance of Professor Angus Rockett in providing SIMS depth profiling results.

References

[1] R.M.A. Azzam, N.M. Bashara, Ellipsometry and Polarized Light, North-Holland, Amsterdam, The Netherlands, 1977.
[2] H. Fujiwara, Spectroscopic Ellipsometry: Principles and Applications, John Wiley & Sons, Chichester, UK, 2007.
[3] J. Li, R.W. Collins, M.N. Sestak, P. Koirala, N.J. Podraza, S. Marsillac, A.A. Rockett, in: D. Abou-Ras, T. Kirchartz, U. Rau (Eds.), Advanced Characterization Techniques for Thin Film Solar Cells, second ed., Wiley-VCH, Weinheim, Germany, 2016, pp. 215–256.
[4] J. Nelson, The Physics of Solar Cells, Imperial College, London, UK, 2003.
[5] J. Krč, M. Topič, Optical Modeling and Simulation of Thin-Film Photovoltaic Devices, Taylor & Francis, Oxford, UK, 2013.
[6] R.W. Collins, A.S. Ferlauto, in: H.G. Tompkins, E.A. Irene (Eds.), Handbook of Ellipsometry, William Andrew, Norwich, NY, 2005, pp. 93–235.
[7] G.E. Jellison, Jr., in: H.G. Tompkins, E.A. Irene (Eds.), Handbook of Ellipsometry, William Andrew, Norwich, NY, 2005, pp. 237–296.
[8] J. Chen, J. Li, C. Thornberry, M.N. Sestak, R.W. Collins, J.D. Walker, S. Marsillac, A.R. Aquino, A. Rockett, in: Proceedings of the 34th IEEE Photovoltaic Specialists Conference, Philadelphia, PA, June 7–12, 2009, IEEE, New York, NY, 2009, pp. 1748–1753.
[9] J. Chen, P. Aryal, J. Li, M.N. Sestak, L.R. Dahal, Z. Huang, R.W. Collins, in: Proceedings of the 37th IEEE Photovoltaic Specialists Conference, Seattle, WA, June 19–24, 2011, IEEE, New York, NY, 2011, pp. 3486–3491.
[10] P. Aryal, J. Chen, Z. Huang, L.R. Dahal, M.N. Sestak, D. Attygalle, R. Jacobs, V. Ranjan, S. Marsillac, R.W. Collins, in: Proceedings of the 37th IEEE Photovoltaic Specialists Conference, Seattle, WA, June 19–24, 2011, IEEE, New York, NY, 2011, pp. 2241–2246.
[11] A.-R.A. Ibdah, Optical Physics of Cu(In,Ga)Se_2 Solar Cells and Their Layer Components, Ph.D. Dissertation, University of Toledo, Toledo, OH, 2016.
[12] A.S. Ferlauto, G.M. Ferreira, C. Chen, P.I. Rovira, C.R. Wronski, R.W. Collins, X. Deng, G. Ganguly, in: R.D. McConnell, V.K. Kapur (Eds.), Photovoltaics for the 21st Century II, Electrochemical Society; Pennington, NJ, 2001, pp. 199–228.
[13] G.M. Ferreira, A.S. Ferlauto, P.I. Rovira, C. Chen, H.V. Nguyen, C.R. Wronski, R.W. Collins, in: J.B. Boyce, J.D. Cohen, R.W. Collins, J. Hanna, M. Stutzmann (Eds.), Amorphous and Heterogeneous Silicon-Based Films - 2001, 664, MRS, Warrendale, PA, 2001 MRS Symp. Proc., A24.6:1-6.
[14] F. Leblanc, J. Perrin, J. Schmitt, J. Appl. Phys. 75 (1994) 1074–1087.
[15] P.I. Rovira, R.W. Collins, J. Appl. Phys. 85 (1999) 2015–2024.
[16] C. Chen, C. Ross, N.J. Podraza, C.R. Wronski, R.W. Collins, in: Proceedings of the 31st IEEE Photovoltaic Specialists Conference, Orlando, FL, January 3–7, 2005, IEEE, New York, NY, 2005, pp. 1524–1527.
[17] G. Rajan, A.-R. Ibdah, K. Aryal, R.W. Collins, S. Marsillac, in: Proceedings of the 39th IEEE Photovoltaic Specialists Conference, Tampa, FL, June 16–21, 2013, IEEE, New York, NY, 2013, pp. 2026–2028.
[18] P. Aryal, Z. Huang, S. Marsillac, N.J. Podraza, R.W. Collins, in: Proceedings of the 42nd IEEE Photovoltaic Specialists Conference, New Orleans, LA, June 14–19, 2015, IEEE, New York, NY, 2015, pp. 1–4. Paper 735–6311.
[19] P. Koirala, J. Li, H.P. Yoon, P. Aryal, S. Marsillac, A.A. Rockett, N.J. Podraza, R.W. Collins, Prog. Photovolt. Res. Appl. 24 (2016) 1055–1067.
[20] A.-R.A. Ibdah, P. Pradhan, P. Aryal, N.J. Podraza, S. Marsillac, R.W. Collins, in: Proceedings of the 43rd IEEE Photovoltaic Specialists Conference, Portland, OR, June 5–10, 2016, IEEE, New York, NY, 2016, pp. 3391–3395.
[21] T. Hara, T. Maekawa, S. Minoura, Y. Sago, S. Niki, H. Fujiwara, Phys. Rev. Appl. 2 (2014) 1–17 Paper 034012.
[22] A.-R. Ibdah, P. Koirala, P. Aryal, P. Pradhan, S. Marsillac, A.A. Rockett, N.J. Podraza, R.W. Collins, Appl. Surf. Spectrosc. B 421 (2017) 601–607.
[23] M.A. Green, Y. Hishikawa, W. Warta, E.D. Dunlop, D.H. Levi, J. Hohl-Ebinger, A.W.H. Ho-Baillie, Prog. Photovolt. Res. Appl. 25 (2017) 668–676.
[24] W.N. Shafarman, S. Siebentritt, L. Stolt, in: A. Luque, S. Hegedus (Eds.), Handbook of Photovoltaic Science and Engineering, second ed., John Wiley & Sons, New York, NY, 2011, pp. 546–599.
[25] P. Aryal, P. Pradhan, D. Attygalle, A.-R. Ibdah, K. Aryal, V. Ranjan, S. Marsillac, N.J. Podraza, R.W. Collins, IEEE J. Photovolt. 4 (2014) 333–339.
[26] J. Li, J. Chen, R.W. Collins, Appl. Phys. Lett. 97 (2010) 181909:1–3.
[27] J. Li, J. Chen, R.W. Collins, Appl. Phys. Lett. 99 (2011) 061905:1-3.
[28] P. Pradhan, P. Aryal, A.-R. Ibdah, P. Koirala, J. Li, N.J. Podraza, A.A. Rockett, S. Marsillac, R.W. Collins, in: Proceedings of the 42nd IEEE Photovoltaic Specialists Conference, New Orleans, LA, June 14–19, 2015, IEEE, New York, NY, 2015 Paper 735–5890:1–4.
[29] P. Pradhan, Real Time Spectroscopic Ellipsometry Analysis of the Three Stages of Cu($In_{1-x}Ga_x$)Se_2 co-Evaporation, Ph.D. Dissertation, University of Toledo, Toledo, OH, 2017.
[30] P. Aryal, Optical and Photovoltaic Properties of Copper Indium-Gallium Diselenide Materials and Solar Cells, Ph.D. Dissertation, University of Toledo, Toledo, OH, 2014.
[31] P. Aryal, A.-R. Ibdah, P. Pradhan, D. Attygalle, P. Koirala, N.J. Podraza, S. Marsillac, R.W. Collins, J. Li, Prog. Photovolt. Res. Appl. 24 (2016) 1200–1213.
[32] M.I. Alonso, K. Wakita, J. Pascual, M. Garriga, N. Yamamoto, Phys. Rev. B 63 (2001) 075203: 1–13.
[33] P. Hoffmann, K. Horn, A.M. Bradshaw, R.L. Johnson, D. Fuchs, M. Cardona, Phys. Rev. B 47 (1993) 1639–1642.
[34] G.E. Jellison, Jr., L.A. Boatner, Phys. Rev. B 58 (1998) 3586–3589.
[35] T.M. Cotter, M.E. Thomas, W.J. Tropf, in: E.D. Palik (Ed.), Handbook of Optical Constants of Solids II, Academic, New York, NY, 1991, pp. 899–917.
[36] J. Li, S. Glynn, L. Mansfield, M. Young, Y. Yan, M. Contreras, R. Noufi, F.L. Terry Jr., D. Levi, in: Proceedings of the 37th IEEE Photovoltaic Specialists Conference, Seattle, WA, June 19–24, 2011, IEEE, New York, NY, 2011, pp. 2749–2752.
[37] G. Czack, W.-D. Fleischmann, D. Gras, V. Haase, G. Kirschstein, Mo Molybdenum Physical Properties; Part 2. Electrochemistry, Springer, Berlin, Germany, 1987.
[38] S. Ninomiya, S. Adachi, J. Appl. Phys. 78 (1995) 1183–1190.
[39] M.M. Junda, C.R. Grice, I. Subedi, Y. Yan, N.J. Podraza, J. Appl. Phys. 120 (2016) 015306:1-8.
[40] J.A. Woollam, B.D. Johs, C.M. Herzinger, J.N. Hilfiker, R.A. Synowicki, C.L. Bungay, in: G.A. Al-Jumaily (Ed.), Optical Metrology: A Critical Review, Proc. SPIE, 10294, SPIE, Bellingham, WA, 1999, pp. 3–28.
[41] B.D. Johs, J.A. Woollam, C.M. Herzinger, J.N. Hilfiker, R.A. Synowicki, C.L. Bungay, in: G.A. Al-Jumaily (Ed.), Optical Metrology: A Critical Review, Proc. SPIE, 10294, SPIE, Bellingham, WA, 1999, pp. 29–58.
[42] E. Burstein, Phys. Rev. 93 (1954) 632–633.
[43] T.S. Moss, Proc. Phys. Soc. (London) B 67 (1954) 775–782.
[44] P. Pradhan, P. Aryal, A.-R. Ibdah, K. Aryal, J. Li, N.J. Podraza, S. Marsillac, R.W. Collins, in: Proceedings of the 40th IEEE Photovoltaic Specialists Conference, Denver, CO, June 8–13, 2014, IEEE, New York, NY, 2014, pp. 2060–2065.
[45] L.A.A. Pettersson, L.S. Roman, O. Inganäs, J. Appl. Phys. 86 (1999) 487–496.
[46] Z. Huang, J. Chen, M.N. Sestak, D. Attygalle, L.R. Dahal, M.R. Mapes, D.A. Strickler, K.R. Kormanyos, C. Salupo, R.W. Collins, in: Proceedings of the 35th IEEE Photovoltaic Specialists Conference, Honolulu, HI, June 20-25, 2010, IEEE, New York, NY, 2010, pp. 1678–1683.
[47] A. Shan, M. Fried, G. Juhász, C. Major, O. Polgár, A. Németh, P. Petrik, L.R. Dahal, J. Chen, Z. Huang, N.J. Podraza, R.W. Collins, IEEE J. Photovolt. 4 (2013) 355–361.